energy&fuels

pubs.acs.org/EF

Article

Optimization and Performance Analysis of Inorganic Lead-Free $CsSnBr_3$ Perovskite Solar Cells Using Diverse Electron Transport Materials

Shazia Akhtar Dar and Brajendra Singh Sengar*

Cite This: *Energy Fuels* 2024, 38, 8229−8248

Read Online

ACCESS | Metrics & More | Article Recommendations | Supporting Information

ABSTRACT: The rapid enhancement in the power conversion efficiency of perovskite solar cells (PSCs) within a short time frame has introduced challenges related to the instability and toxicity linked with lead (Pb), impeding their progress toward commercial viability. In response, the exploration of Pb-free alternatives, such as $CsSnBr_3$, has garnered substantial research attention. $CsSnBr_3$ stands out as a highly promising contender for fulfilling the role of an absorber layer in solar cell technology, distinguished by its economical nature, robust stability, and impressive efficiency. In this study, $CsSnBr_3$ is employed as an absorber layer, Cu_2O as the hole transport layer (HTL), and TiO_2, PCBM, WS_2, ZnO, SnO_2, and IGZO as electron transport layers (ETLs). This work focuses on enhancing the photovoltaic (PV) performance parameters of $CsSnBr_3$-based PSCs using SCAPS-1D numerical simulation. This is achieved by optimizing characteristics (thickness, doping, and defect density) of the light absorber layer, ETLs, and HTL. Additionally, the effects of doping and defect density (N_t) on the PV performance at $CsSnBr_3$/ETL and HTL/$CsSnBr_3$ interfaces are investigated. The device architecture's performance was significantly influenced by the absorber layer's thickness, acceptor density, defect density, and the combination of various ETLs and HTLs. Optimized devices employing TiO_2, PCBM, WS_2, ZnO, SnO_2, and IGZO ETLs exhibited PCEs of 21.64, 21.94, 22.43, 21.94, 21.94, and 21.88%, respectively. Moreover, the study included the illustration of capacitance effects and Mott−Schottky (M−S) analysis for the six optimized devices, complemented by the computation of corresponding $J-V$ and QE characteristics. The PV performance obtained from this thorough analysis is then compared with previously published theoretical and experimental results for $CsSnBr_3$-based PSCs. The performance of the top six devices is validated and compared using the wxAMPS simulation tool. By employing a variety of analytical techniques and theoretical simulations, an optimized configuration is developed, leading to the achievement of the highest reported efficiency to date at 22.43% using any simulation method for indium-doped tin oxide/TiO_2/$CsSnBr_3$/Cu_2O/Au configuration.

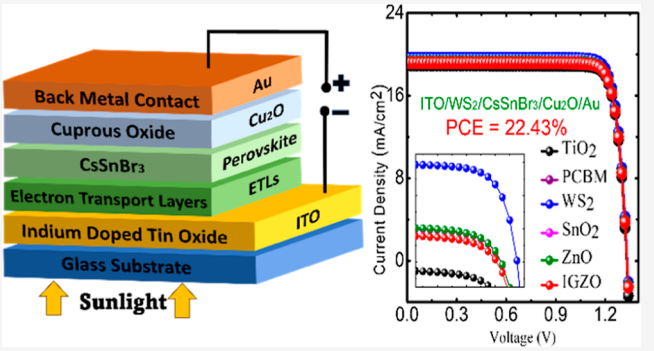

1. INTRODUCTION

The perovskite solar cell (PSC) has emerged as a highly promising photovoltaic technology, achieving a power conversion efficiency (PCE) that surpasses 25% in a single-junction architecture. This impressive level of efficiency positions PSCs as formidable competitors to traditional silicon solar cells. Remarkably, PSCs are on the verge of commercialization, marking a significant milestone within just over a decade since their inception.[1,2] However, the journey of PSCs toward industrialization faces significant hurdles, primarily revolving around the stability of the device in ambient air under illumination and concerns regarding the toxicity of the materials employed.[3−8] To date, the most effective formulation for PSCs comprises a synergistic blend of methylammonium, formamidinium (FA), and cesium (Cs^+) strategically placed in the A cation site.[9−13] Simultaneously, lead (Pb) is positioned in the B cation site, while iodine(I), chlorine (Cl), and bromine (Br) are integrated into the X anion site within the well-defined ABX_3 perovskite structure.[14] Nevertheless, the presence of toxic and heavy metals, particularly lead, throughout the lifecycle of PSCs raises significant environmental concerns.[6−8] Despite the high efficiency achieved, the skepticism from both research communities and the industry regarding its future has led to a growing interest in Pb-free perovskite materials. Consequently, researchers are actively exploring alternatives to Pb-containing perovskites for SC applications. Several Pb-free

Received: February 29, 2024
Revised: April 4, 2024
Accepted: April 4, 2024
Published: April 19, 2024

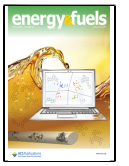

https://doi.org/10.1021/acs.energyfuels.4c00953
Energy Fuels 2024, 38, 8229−8248

perovskite absorber materials are characterized by wide bandgaps, making them viable candidates for replacing their hazardous lead-containing counterparts. The pioneering studies on $CsSnX_3$ perovskites were documented approximately between 2014 and 2017.[15−17] Tin-based perovskite absorber materials are gaining prominence in the research sector due to their properties, which closely resemble those of lead halide perovskites and exhibit high PCE. Nevertheless, a significant challenge that requires attention is the degradation of these devices in ambient atmospheric conditions. In the realm of solar applications, prominent Sn-based perovskites include $MASnI_3$ (1.3 eV), $FASnI_3$ (1.41 eV), $CsSnI_3$ (1.3 eV), and $CsSnBr_3$ (1.75−1.80 eV).[11,18−23] Among these, $CsSnBr_3$ received less attention, primarily because of its wider bandgap,[39] making it a less efficient light absorber for PSCs compared to the other three. Despite this, $CsSnBr_3$ demonstrated greater robustness than $CsSnI_3$. The Pb-free alternative, $CsSnBr_3$, exhibits competitive semiconductor properties, featuring a direct bandgap,[20] improved thermal stability,[12] favorable absorption coefficient,[21] and better carrier lifetime.[24] The development of SnO_2, $SnBr_2$, and $SnBr_4$ can lead to defects in $CsSnBr_3$ perovskite, which raises serious concerns about the stability of Sn-based PSCs. These defects, whether originating during material synthesis or due to exposure to moisture and oxygen, negatively impact both performance and stability.[25] To tackle these challenges, researchers have implemented various strategies. Hartmann et al. investigated the chemical and electronic structures of $CsSnBr_3$ and examined the impact of adding 20 mol % SnF_2 to the precursor solution. The results demonstrated that the addition of SnF_2 improves substrate coverage, reduces Sn^{II} to Sn^{IV} oxidation, and inhibits the formation of secondary Br and Cs species.[26] Despite these efforts, the efficiency remains considerably below the theoretical limit, indicating ample room for enhancing device performance and film stability. In 2015, Sabba et al. showcased an effective approach to elevate the V_{oc} of Sn-based perovskite by introducing Br anions into $CsSnI_{3-x}Br_x$. This incorporation induces a crystal structure shift from orthorhombic to cubic, transitioning from $CsSnI_3$ to $CsSnBr_3$. The modulation of the bandgap through Br-substitution is expected to augment the V_{oc} of $CsSnI_3$ perovskite without the need for an additional reducing agent like SnF_2. Device structures FTO/TiO_2/$CsSnBr_3$/Spiro-OMeTAD/Au and FTO/TiO_2/$CsSnBr_3$:SnF_2/Spiro-OMeTAD/Au demonstrated PCEs of 0.1 and 0.95%, respectively.[27] Song et al. introduced a novel process utilizing a reducing vapor atmosphere during cell preparation with $CsSnBr_3$ as the absorber, yielding significantly improved solar cells with an efficiency of 3.04%. The process reduces Sn^{4+}/Sn^{2+} ratios by over 20%, mitigating carrier recombination and advancing the development of low-cost, Pb-free Sn-based halide PSCs. However, the inclusion of an organic hole transport layer (HTL) poses a challenge to the long-term operational stability.[28] Gupta et al. conducted a study focusing on the influence of SnF_2 in improving the properties of $CsSnBr_3$, resulting in a maximum PCE of 2.1%.[11] Gao et al. reported the synthesis of $CsSnBr_3$ perovskite using a solid-phase reaction. The $CsSnBr_3$ film created through this process exhibited stability in ambient air for 8 days. The novel device structure (FTO/TiO_2/$CsSnBr_3$/MoO_3/Al) demonstrated a PCE of 1.5%.[21] In a study by Kumar et al., the integration of rGO (reduced graphene oxide) nanocomposite was showcased to improve the structural and optical characteristics of pure $CsSnBr_3$. The most favorable SC outcomes were observed with a 3% rGO concentration, yielding key parameters of PCE = 5.27%, V_{oc} = 0.714 V, J_{sc} = 12.04 mA/cm^2, and an FF = 61.32%.[29] Nasrin et al. reported the PSC-based structure, FTO/TiO_2/$CsSnBr_3$/P3HT/Au, using SCAPS-1D. This device structure demonstrated PCE = 17.94%, V_{oc} = 1.3 V, J_{sc} = 18 mA/cm^2, and FF = 74.5%.[24] While Sn-based PSCs have seen rapid experimental progress, there is still untapped potential for improvement by optimizing different parameters and device configurations. This optimization not only provides insights for future experimental enhancements but also serves as a guide. In this investigation, we conducted simulations for a total of 70 (Figure S1) unique combinations [10 HTLs (Table S1) and 7 electron transport layers (ETLs)] of PSC device structures. Subsequently, we identified six optimal devices distinguished by exceptional characteristics and promising performance parameters. This study further delves into the optimization of the performance of these top six structures. This involves examining various optoelectronic properties and assessing the impact of absorber layer, ETL, and HTL thicknesses and interface properties. Additionally, we explore the effects of capacitance, M−S, J−V, and QE characteristics. The performance of the top devices is verified using the wxAMPS simulation tool, and a comparative analysis of SCAPS-1D results with published reports is conducted. By employing a variety of analytical techniques and theoretical simulations, an optimized configuration is developed, leading to the achievement of the highest reported efficiency to date at 22.43% using any simulation method for indium-doped tin oxide (ITO)/TiO_2/$CsSnBr_3$/Cu_2O/Au configuration.

2. NUMERICAL MODELING AND MATERIAL PARAMETERS

2.1. SCAPS-1D Numerical Simulation. SCAPS-1D is a semiconductor device modeling framework developed by the University of Gent to model and simulate PSCs.[30] The primary equations used in SCAPS-1D are Poisson equation (eq 1 as well as the continuity equations for both holes and electrons (eqs 2−3), given as follows

$$\frac{dE}{dx} = -\frac{d^2\varphi}{dx^2} = \frac{q}{\varepsilon_0\varepsilon_r}[p(x) - n(x) + N_D^+(x) - N_A^-(x) + \rho_t(x) - n_t(x)] \quad (1)$$

$$\frac{dp_n}{dt} = G_p - \frac{p_n - p_{n0}}{\tau_p} + p_n\mu_p\frac{dE}{dx} + \mu_p E\frac{dp_n}{dx} + D_p\frac{d^2p_n}{dx^2} \quad (2)$$

$$\frac{dn_p}{dt} = G_n - \frac{n_p - n_{p0}}{\tau_n} + n_p\mu_n\frac{dE}{dx} + \mu_n E\frac{dn_p}{dx} + D_n\frac{d^2n_p}{dx^2} \quad (3)$$

where q represents the electron charge, ε represents the dielectric permittivity, $G_{n/p}$ represents the electron (hole) generation rate, $D_{n/p}$ represents the electron (hole) diffusion coefficients, φ represents the electrostatic potential, and E represents the electric field.

Carrier transport occurs through an efficient interplay of diffusion and drift mechanisms, which can be elucidated in eqs 4 and 5

https://doi.org/10.1021/acs.energyfuels.4c00953
Energy Fuels 2024, 38, 8229−8248

$$J_n(x) = qn\mu_n E + qD_n\frac{dn}{dx} = n\mu_n\frac{dE_{Fn}}{dx} \quad (4)$$

$$J_p(x) = qp\mu_p E - qD_p\frac{dp}{dx} = p\mu_p\frac{dE_{Fp}}{dx} \quad (5)$$

where $\mu_{n/p}$ represents the electron (hole) mobilities and $E_{Fn/Fp}$ is the quasi-Fermi level for electrons (holes).

2.2. wxAMPS Numerical Simulation. In this study, the wxAMPS, 1D SC simulation framework developed by the University of Illinois is used to perform a similar numerical investigation as a supplementary validation of the performance of PSC. In the wxAMPS framework, the 1D Poisson's equation is (6)

$$\frac{d}{dx}\left(-\varepsilon(x)\frac{d\varphi}{dx}\right) = q[p(x) - n(x) + N_D^+(x) - N_A^-(x) + p_t(x) - n_t(x)] \quad (6)$$

where n (p) represents free electrons (holes), n_t (p_t) represents trapped electrons (holes), and N_D^+ (N_A^-) represents ionized donor (acceptor) dopants.

The continuity equation for both free electrons and holes, which describes how the PSC behaves in the various regions of the structure, is as follows (7 and 8)

$$\frac{1}{q}\frac{dJ_n}{dx} = -G_{op}(x) + R(x) \quad (7)$$

$$\frac{1}{q}\frac{dJ_p}{dx} = G_{op}(x) - R(x) \quad (8)$$

where J_n (J_p) represents the electron (hole) current densities, $R(x)$ represents the net rate of recombination, and $G_{op}(x)$ is a function of x, representing the rate of optical generation due to light supplied externally.

2.3. $CsSnBr_3$ PSC Structure. In the majority of perovskite device structures, the light harvesting layer (absorber) is placed between an ETL and HTL. Both these transport layers play a vital role in averting the recombination of photogenerated carriers and enhancing the charge transportation by establishing paths for the separation of carriers, allowing electrons and holes to move from the absorber layer to the electrodes and ultimately reach the external circuit through metal (Au) contacts.

In the present study, a normal (n-i-p) structure for the $CsSnBr_3$-based PSC (Figure 1) with ITO as the front contact, Cu_2O as the HTL, and gold (Au) as the back contact is employed. The charge transport layers TiO_2, PCBM, WS_2, SnO_2, ZnO, and IGZO are used as ETLs. Figure 1b represents the structure of the optimized $CsSnBr_3$-based SC. Figure 1c demonstrates the energy band diagram of the $CsSnBr_3$-based SC where WS_2 is used as the ETL along with Cu_2O HTL, and Figure 1d represents the corresponding energy band alignment.

The input simulation parameters for ETL, $CsSnBr_3$ absorber layer, and HTL required for SCAPS-1D simulation are extracted from relevant literature sources, which are detailed in Tables 1 and S1. Table 2 details the simulation parameters related to interface defect density. The energy band alignment between ITO, different ETLs (TiO_2, PCBM, WS_2, SnO_2, IGZO, and C_{60}), HTL, and back metal contact (Au) is demonstrated in Figure 2. All the simulations were conducted under standard conditions, which include a frequency of 1 MHz and exposure to the AM 1.5G spectrum of sunlight at an ambient temperature of 300 K.

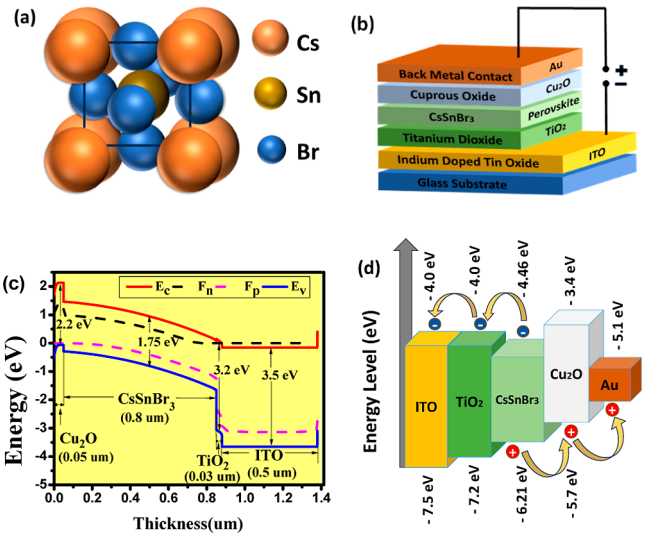

Figure 1. (a) Crystal structure of the $CsSnBr_3$ absorber, (b) PSC device architecture, (c) energy band diagram, and (d) energy band alignment of an optimized PSC.

3. RESULTS AND DISCUSSION

3.1. Verification of the Device Models. To validate the material parameters, our initial emphasis was placed on the examination of a device incorporating TiO_2 as the ETL, $CsSnBr_3$ as the light absorption layer, and Spiro-OMeTAD as the HTL. The energy band diagram of the considered device is presented in Figure 3a, and the simulated $J-V$ curves are illustrated in Figure 3b. The device exhibits a V_{oc} of 0.85 V, J_{sc} of 20.63 mA cm^{-2}, FF of 59.6%, and PCE of 10.45%.

These results align with the experimental findings reported by Chen et al.,[33] thereby reinforcing the integrity of the numerical simulation. As a result, the chosen material parameters for the device model are justified, providing a solid foundation to proceed with subsequent experiments centered around this specific device setup. A minor disparity between the experimental outcomes and our computed results lies in the utilization of ITO and Au layers as front and back electrodes in our present research. Notably, the thickness of these front and back contacts remains fixed. Conversely, in the experimental investigation, these layers were used with specifically tailored thicknesses to suit the device configuration.

3.2. Effect of the Absorber Layer Thickness and Defect Density on PV Performance. The optimized thickness of the absorber layer as well as defect density (N_t) play an important role in determining the performance of the SC. Figures 4a–f, 5a–f, 6a–f, and 7a–f show the impact of absorber layer thickness and N_t through contour plots on the PCE, V_{oc}, J_{sc}, and FF, respectively, for the structures under investigation. The absorber layer thickness is varied from 200 to 1200 nm, and N_t is adjusted from 1×10^{13} to 1×10^{20} cm^{-3} to determine the optimal absorber defect density and thickness.

In contour plots 4a–f, all the six optimized ETL-based structures exhibit a consistent trend: as the absorber thickness increases, the PCE rises, while a simultaneous increase in defect density results in a decrease in PCE. Contour plots

https://doi.org/10.1021/acs.energyfuels.4c00953
Energy Fuels 2024, 38, 8229–8248

Table 1. Initial Input Simulation Parameters for ITO, ETLs, HTL, and $CsSnBr_3$ Absorber Layer[24,31,32]

parameters	ITO	TiO_2	PCBM	WS_2	SnO_2	ZnO	IGZO	Cu_2O	$CsSnBr_3$
thickness (nm)	500	30	50	100	100	50	30	50	800[a]
E_g (eV)	3.5	3.2	2	1.8	3.6	3.3	3.05	2.2	1.75
χ (eV)	4	4	3.9	3.95	4	4	4.16	3.4	4.07
ε_r	9	9	3.9	13.6	9	9	10	7.5	5.9
N_C (1/cm^3)	2.2×10^{18}	2×10^{18}	2.5×10^{21}	1×10^{18}	2.2×10^{18}	3.7×10^{18}	5×10^{18}	2×10^{19}	1×10^{19}
N_V (1/cm^3)	1.8×10^{19}	1.8×10^{19}	2.5×10^{21}	2.4×10^{19}	1.8×10^{19}	1.8×10^{19}	5×10^{18}	1×10^{19}	1×10^{19}
μ_n (cm^2 V^{-1} s^{-1})	20	20	0.2	100	100	100	15	200	2
μ_n (cm^2 V^{-1} s^{-1})	10	10	0.2	100	25	25	0.1	8600	2
N_A (1/cm^3)	0	0	0	0	0	0	0	1×10^{18}	1×10^{15}[a]
N_D (1/cm^3)	1×10^{21}	9×10^{16}	2.93×10^{17}	1×10^{18}	1×10^{17}	1×10^{18}	1×10^{17}	0	0
N_t (1/cm^3)	1×10^{15}[a]	1×10^{15}[a]	1×10^{15}[a]	1×10^{15}[a]	1×10^{15}[a]	1×10^{15}[a]	1×10^{15}[a]	1×10^{15}[a]	1×10^{15}[a]

[a]In this study, these parameters are kept constant during the first optimization to obtain an optimal ETL and HTL.

Table 2. Input Parameters of Interface Defect Layers[31,32]

interface	defect type	energetic distribution	capture cross section: electrons/holes (cm^2)	reference for defect energy level	energy with respect to reference (eV)	total density (cm^{-3}) (integrated over all energies)
ETL/$CsSnBr_3$	neutral	single	1.0×10^{-17}	above the VB maximum	0.6	1.0×10^{10}
			1.0×10^{-18}			
HTL/$CsSnBr_3$	neutral	single	1.0×10^{-18}	above the VB maximum	0.6	1.0×10^{10}
			1.0×10^{-19}			

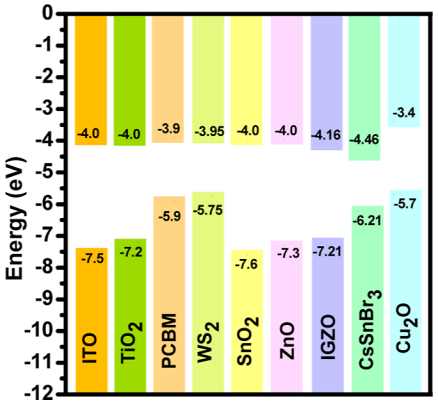

Figure 2. Energy band alignment between ITO, different ETLs (TiO_2, PCBM, WS_2, SnO_2, ZnO, and IGZO), HTL (Cu_2O), and back metal contact (Au).

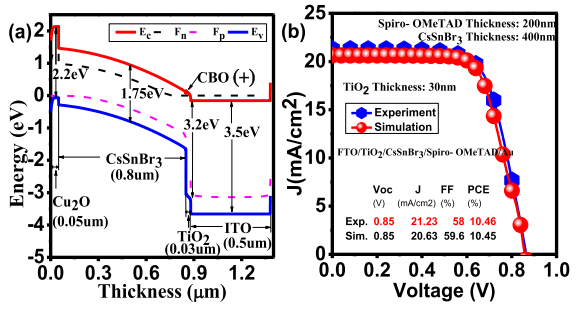

Figure 3. (a) Energy band schematic and (b) experimental and modeled $J-V$ curves of the ITO/TiO_2/$CsSnBr_3$/Spiro-OMeTAD/Au PSCs.

reveal that PCE exhibits a strong sensitivity to changes in N_t. As N_t increases from 1×10^{13} to 1×10^{14} cm^{-3} across all device structures, PCE initiates a decline, and as N_t continues to increase, PCE deteriorates further. TiO_2-, PCBM-, WS_2-, SnO_2-, ZnO-, and IGZO-based PSCs demonstrate the highest PCE of 23.94, 23.80, 23.98, 23.93, 23.90, and 23.94%, respectively, with absorber thickness set at 1200 nm and N_t set at 1×10^{13} cm^{-3}. The increase in N_t significantly impairs the PCE in all the six optimized PSC-based structures. For TiO_2-, PCBM-, WS_2-, SnO_2-, ZnO-, and IGZO-based PSC structures, PCE reduces from 23.93 to 0.014%, 23.8 to 0.012%, 23.98 to 0.008%, 23.93 to 0.014%, 23.94 to 0.013%, and 23.90 to 0.016%, respectively, as N_t increases from 1×10^{14} to 1×10^{20} cm^{-3} with an absorber length of 1200 nm. The contour plots clearly demonstrate that decreasing the thickness of the absorber leads to a drop in the PCE. This phenomenon arises due to the utilization of thinner absorber layers, which allows a significant portion of light (photons) to traverse the material without being absorbed. As a result, there is a decrease in the generation of electron−hole (e−h) pairs, leading to a subsequent fall in the PCE. In contrast, as the thickness of the absorber grows, there is a corresponding increase in optical absorption and the formation of e−h pairs, resulting in an improved PCE.[34] Nevertheless, once the absorber thickness exceeds the optimal value, PCE begins to decrease. This loss is attributed to increased recombination caused by a longer diffusion length.[35,36] Defect density in PSCs hinder the SC performance by acting as sites where carriers recombine and as pathways for ion migration when exposed to light.[37]

In contour plots 5a−f, the V_{oc} for various ETL-based structures is depicted. It is evident that an increase in both the absorber thickness and N_t leads to a reduction in V_{oc}. When N_t increases from 1×10^{13} to 1×10^{14} cm^{-3} for all device structures, V_{oc} begins to decrease, and further increases in N_t worsen V_{oc}. Among the PSCs studied, TiO_2-, WS_2-, SnO_2-, ZnO-, and IGZO-based structures exhibit the highest V_{oc} values, measuring 1.465, 1.471, 1.465, 1.466, and 1.454 V, respectively. Conversely, the PCBM-based structure shows the lowest V_{oc} of 1.381 V, given an absorber thickness of 100 nm and N_t set at 1×10^{13} cm^{-3}. Increasing N_t and absorber thickness significantly reduces V_{oc} in all the six optimized PSC-

https://doi.org/10.1021/acs.energyfuels.4c00953
Energy Fuels 2024, 38, 8229−8248

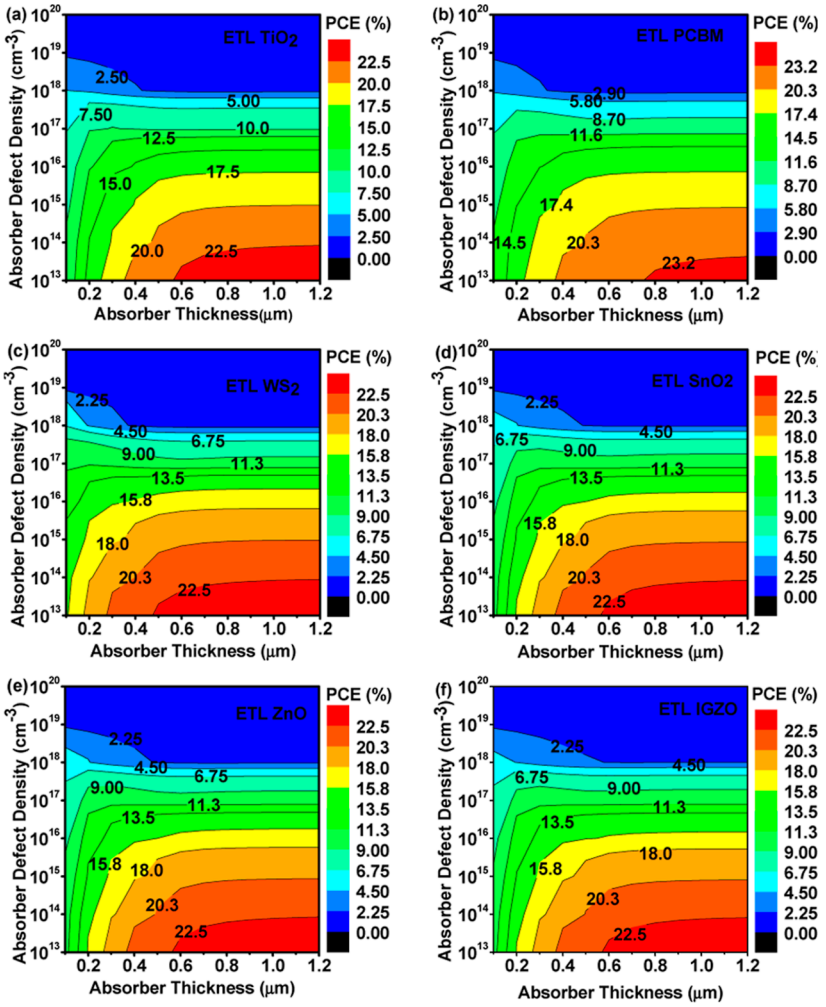

Figure 4. Contour plots depict the influence of absorber defect density and absorber thickness on PCEs for different ETLs.

based structures. For TiO_2-, PCBM-, WS_2-, SnO_2-, ZnO-, and IGZO-based PSC structures, V_{oc} decreases from their respective initial values to ~0.697 V as N_t increases from 1 × 10^{13} to 1 × 10^{20} cm^{-3} with an absorber thickness of 1000 nm.

In contour plots 6a–f, J_{sc} values for various ETL-based structures are displayed. It is clear that an increase in N_t leads to a reduction in J_{sc}. The contour plots further reveal that as the absorber layer thickness is increased from 100 to 1200 nm and N_t is simultaneously raised from 1 × 10^{13} to 1 × 10^{17} cm^{-3}, there is no significant decrease in J_{sc}. However, once N_t surpasses 1 × 10^{17} cm^{-3}, J_{sc} experiences a substantial drop, regardless of the absorber thickness. TiO_2-, PCBM-, WS_2-, SnO_2-, ZnO-, and IGZO-based PSC structures exhibited the highest J_{sc}, reaching 19.8 mA/cm^2 when the absorber thickness was set at 1200 nm. This value decreased to 0.05 mA/cm^2 when N_t was increased to 1 × 10^{20} cm^{-3}.

In contour plots 7a–f, FF values for various ETL-based structures are displayed. The contour plots provide an insight into how altering the absorber thickness along with N_t affects the FF of PSCs. When N_t is in the range of 1 × 10^{13} to 1 × 10^{15} cm^{-3}, the FF decreases gradually. However, once N_t surpasses 1 × 10^{15} cm^{-3}, there is a sudden and significant decline in the FF across all absorber layer thicknesses within the six optimized structures. Devices based on TiO_2, PCBM, WS_2, SnO_2, ZnO, and IGZO exhibited the highest FF values, measuring 85.2, 88.99, 86.14, 85.25, 85.12, and 85.49%, respectively, for an absorber thickness of 100 nm and N_t set at 1 × 10^{13} cm^{-3}. This value was reduced to approximately 38–36% from its initial value when the absorber thickness remained at 100 nm and N_t was raised to 1 × 10^{20} cm^{-3} for all device structures.

3.3. Effect of the Absorber Defect Density and Defect Energy Level on PV Performance. In this section, the influence of $CsSnBr_3$ defect density (N_t) and defect energy level (E_t) on the performance of PSC is investigated. The performance of PSCs is contingent upon two pivotal processes: the generation of charge carriers and their subsequent recombination. When PSCs are exposed to sunlight, the absorber layer triggers the creation of photoinduced carriers, encompassing both electrons and holes. These newly formed carriers are then channeled toward the electrode and directed into the external circuit. However, during the collection of these photoinduced charge carriers, a substantial portion is lost due to poor quality of the absorber layer. This diminished quality results in a higher defect density, which in turn accelerates the recombination rate within low-quality absorber films. This increased recombination rate not only curtails the distance over which charge carriers can travel (diffusion length) but also shortens their lifespan. To shed light on the underlying recombination mechanisms and how they are

https://doi.org/10.1021/acs.energyfuels.4c00953
Energy Fuels 2024, 38, 8229–8248

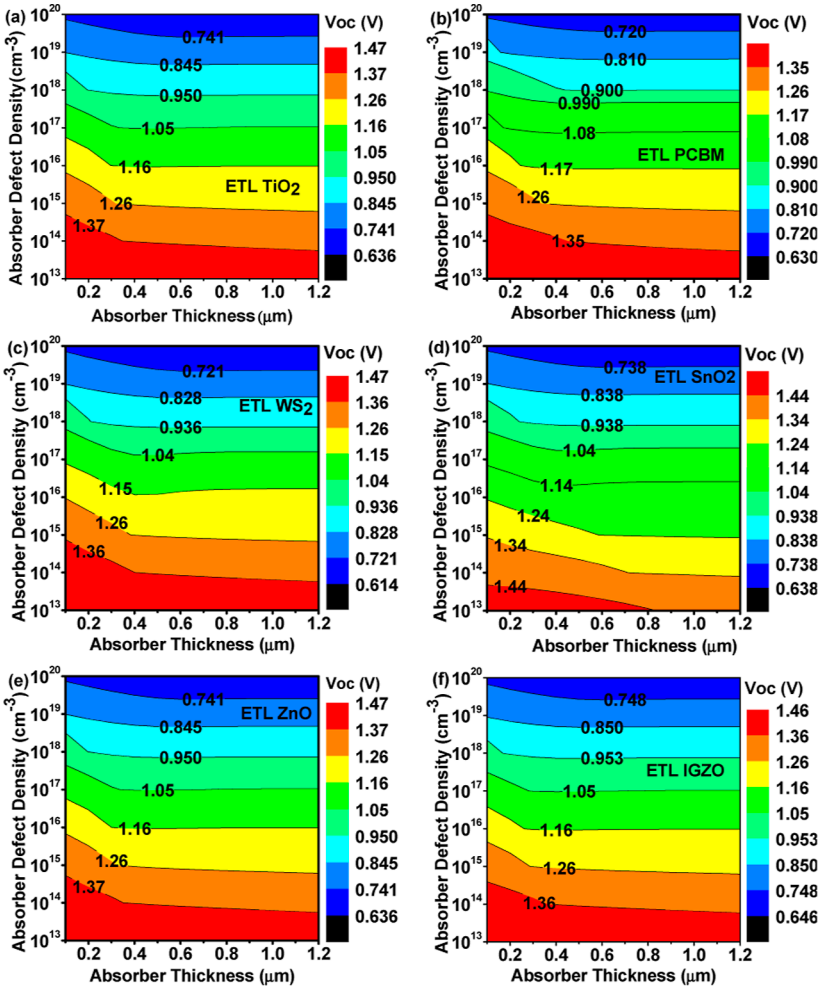

Figure 5. Contour plots depict the influence of absorber defect density and absorber thickness on V_{oc} for different ETLs.

influenced by defect density, eq 9 delineates the Shockley–Read–Hall (SRH) recombination process as[38]

$$\mathcal{R}^{\mathrm{SRH}} = \frac{V_t \sigma_n \sigma_p N_t [np - n_i^2]}{\sigma_p [p + p_1] + \sigma_n [n + n_1]} \tag{9}$$

where N_t is the defect density, τ_p (τ_n) defines the lifetime of holes (electrons),and σ_p (σ_n) specifies the capture cross section of holes (electrons).

Parameters p_1 and n_1 introduce the dependency of the recombination rate on the trapping energy level, E_t, in the following manner[39]

$$p_1 = N_v \, e^{(E_v - E_t)/kT} \tag{10}$$

$$n_1 = N_c \, e^{(E_t - E_c)/kT} \tag{11}$$

where E_t is the trap energy level.

In eq 9, it is observed that the $\mathcal{R}^{\mathrm{SRH}}$ effect is directly linked to the N_t within the light harvesting layer. Haider and colleagues found that reducing N_t in the absorber layer results in an increase in diffusion length. This phenomenon, in turn, enhances the overall performance of PSCs.[39] To assess the impact of N_t on the device's performance, the carrier diffusion length (L_D) in eq 12 is considered, incorporating the SRH effect ($\mathcal{R}^{\mathrm{SRH}}$) and carrier lifetime ($\tau_{(e,h)}$) as[38,39]

$$L_D = \sqrt{\frac{\mu_{(e,h)} \mathcal{R}^{SRH} T \tau_{(e,h)}}{q}} \text{ and } \tau_{(e,h)} = \frac{1}{N_t \sigma_{n,p} V_T} \tag{12}$$

Analyzing eqs 9–12, we can draw the conclusion that an increase in defect density increases the recombination rate, subsequently leading to a reduction in the diffusion length and carrier lifetime, thereby reducing the number of carriers reaching the contacts. Therefore, it becomes quite evident that as the value of N_t increases, the degradation in the overall performance of PSCs becomes more pronounced.

Figures 8a–f, 9a–f, 10a–f, and 11a–f demonstrate the contour plots of the important PV performance parameters: PCE, V_{oc}, J_{sc}, and FF, respectively, with the simultaneous variation of absorber defect density (N_t) and defect energy level (E_t) for different ETLs in our investigation. The N_t spans a range from 1×10^{14} to 1×10^{19} cm^{-3}, while the E_t extends from 0 to 1.2 eV. Analysis through contour plots 8a–f reveals a consistent trend: when simultaneously adjusting both N_t and E_t, the PCE decreases across all six ETL-based device structures. In the case of a TiO_2-based device, the highest PCE achieved is 24.83%, occurring when E_t is 0 eV and N_t is 1×10^{14} cm^{-3}. However, as N_t increases to 1×10^{19} cm^{-3} while keeping E_t constant at 0 eV, the PCE drops to 20.36%. Furthermore, when N_t is raised to 1×10^{19} cm^{-3} and E_t is increased to 1.2 eV from its initial value, the PCE decreases to 21.76%. Additionally, a shift in E_t from 0 to 0.6 eV, with N_t

https://doi.org/10.1021/acs.energyfuels.4c00953
Energy Fuels 2024, 38, 8229–8248

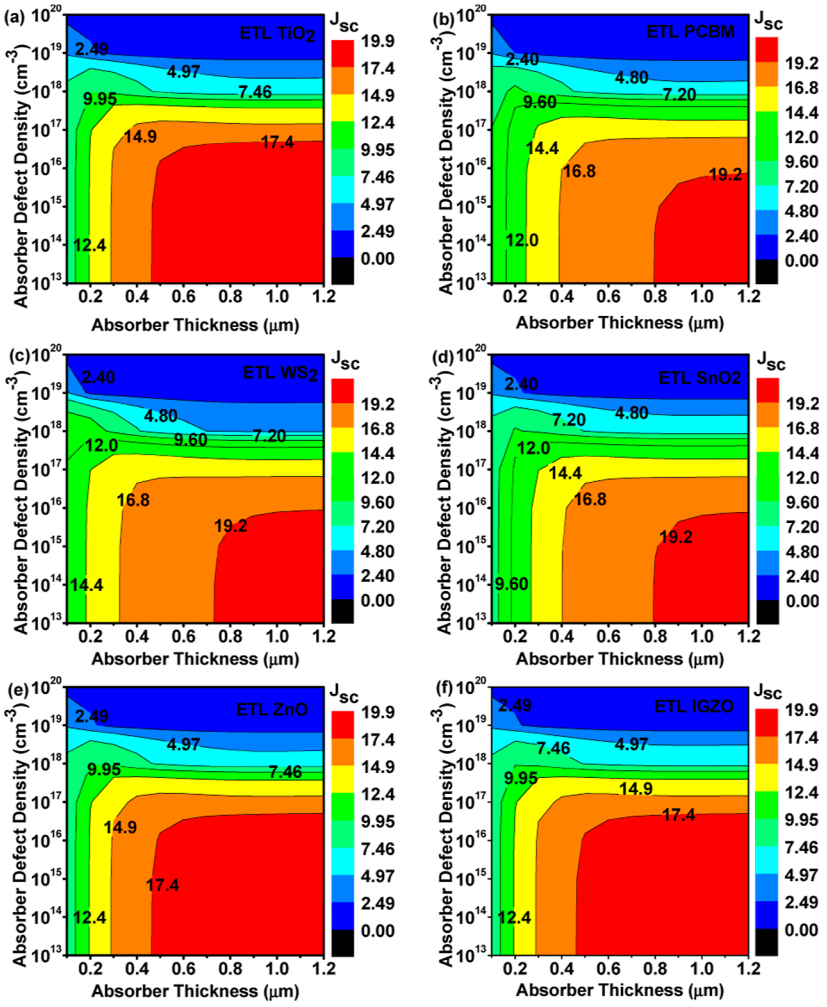

Figure 6. Contour plots depict the influence of absorber defect density and absorber thickness on J_{sc} for different ETLs.

exceeding 1×10^{16} cm^{-3}, results in a significant decline in PCE. However, when E_t surpasses 0.6 eV, there is no substantial change in PCE for any value of N_t, as indicated by the contour plots. This consistent pattern is observed across all six PSC-based structures. For instance, in a TiO_2-based structure, when E_t is at 0 eV and N_t is 1×10^{14} cm^{-3}, the PCE reaches 24.83%. As E_t increases from 0 to 0.6 eV, the PCE decreases to 21.765%, and once the E_t surpasses 0.6 eV, the PCE remains relatively stable. With N_t of 1×10^{19} cm^{-3} and an E_t of 1.2 eV, the PCE drops to 0.17%. In the case of PCBM-, WS_2-, SnO_2-, ZnO-, and IGZO-based devices, the highest PCE achieved is 24.13, 24.99, 24.82, 24.83, and 24.79%, respectively, when E_t is set at 0 eV and N_t at 1×10^{14} cm^{-3}.

Contour plots 9a–f provide insights into how an increase in N_t and E_t results in a decrease in V_{oc} for all the six optimized structures. In devices based on TiO_2, PCBM, WS_2, SnO_2, ZnO, and IGZO, the highest V_{oc} values achieved are 1.50, 1.40, 1.49, 1.50, 1.50, and 1.49 V, respectively, when N_t is set at 1×10^{14} cm^{-3} and E_t is at 0 eV. However, when N_t is increased to 1×10^{19} cm^{-3} and E_t is raised to 1.2 eV, V_{oc} decreases to 0.764, 0.757, 0.740, 0.764, 0.763, and 0.77 V, respectively, from their initial values. However, when E_t surpasses 0.6 eV, there is no substantial change in V_{oc} for any value of N_t, as indicated by the contour plots. This consistent pattern is observed across all six PSC-based structures. A study by Soucase et al. highlights the significant influence of the N_t on V_{oc}.[40] From a practical standpoint, the N_t in the absorber layer depends on factors such as formation energy and chemical potential, which, in turn, are influenced by precursors, partial pressure, and synthesis temperature. Defects with low formation energy only create shallow levels, leading to longer carrier diffusion lengths (L_D) and higher V_{oc}. Conversely, defects with deep energy levels have higher formation energy, adversely affecting L_D and V_{oc}. Experimental and simulation results confirm the existence of unusually shallow defect levels, which are associated with long L_D and high V_{oc}. The quality of the absorber layer determines the L_D, and if L_D exceeds the thickness of the absorber layer, it results in superior device performance. The relationship between L_D, J_o, and V_{oc} can be summarized as follows[41]

$$J_o \approx q\frac{Dn_i^2}{L_D N} \tag{13}$$

$$V_{oc} = \frac{KT}{q}\ln\left(\frac{J_{sc}}{J_o} + 1\right) \tag{14}$$

where J_o is the recombination current.

Based on eqs 13 and 14, it can be inferred that reducing N_t leads to a decrease in J_o, which enhances L_D and, consequently improving V_{oc}, aligning with the results obtained.

https://doi.org/10.1021/acs.energyfuels.4c00953
Energy Fuels 2024, 38, 8229–8248

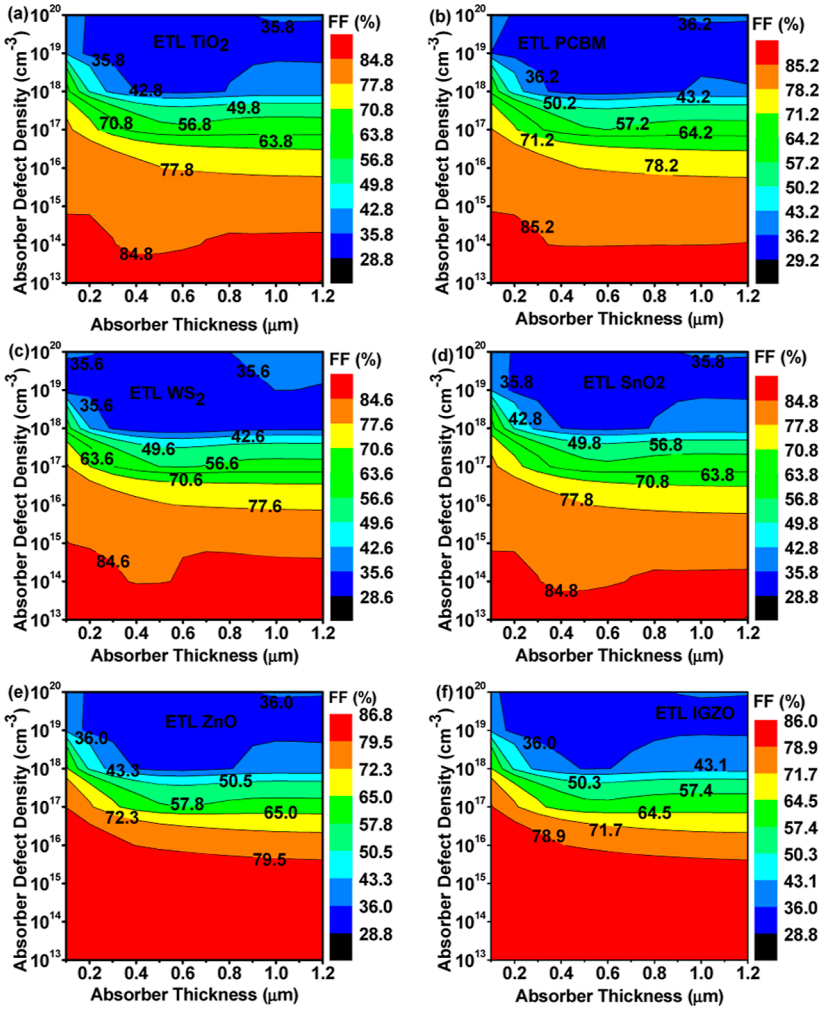

Figure 7. Contour plots depict the influence of absorber defect density and absorber thickness on FF for different ETLs.

Contour plots 10a–f illustrate a significant reduction in J_{sc} values when both N_t and E_t of the absorber layer vary simultaneously. In the case of devices utilizing TiO_2, PCBM, WS_2, SnO_2, ZnO, and IGZO, the highest J_{sc} values obtained are 19.23, 19.21, 19.37, 19.22, 19.22, and 19.22 mA/cm^2, respectively, when N_t is set at 1×10^{14} cm^{-3} and E_t is at 0 eV. However, when N_t is increased to 1×10^{19} cm^{-3} and E_t is raised to 1.2 eV, J_{sc} decreases to 0.66, 0.57, 0.40, 0.67, 0.65, and 0.77 mA/cm^2, respectively, from their initial values. Nevertheless, when E_t exceeds 0.6 eV, J_{sc} remains relatively constant for any value of N_t, as indicated by the contour plots across all the six PSC-based structures.

Contour plots 11a–f demonstrate a significant reduction in FF values when both N_t and E_t of the absorber layer vary simultaneously. In the case of devices utilizing TiO_2, PCBM, WS_2, SnO_2, ZnO, and IGZO, the highest FF values obtained are 85.88, 89.59, 86.6, 85.9, 85.87, and 86.24%, respectively, when N_t is set at 1×10^{14} cm^{-3} and E_t is at 0 eV. However, when N_t is increased to 1×10^{19} cm^{-3} and E_t is raised to 1.2 eV, FF decreases to 32.68, 33.23, 33.91, 32.66, 32.68, and 33.37%, respectively, from their initial values. Nevertheless, when E_t exceeds 0.6 eV, FF remains relatively constant for any value of N_t, as indicated by the contour plots across all the six PSC-based structures.

3.4. Influence of Layer Thickness on PV Performance.

3.4.1. Influence of $CsSnBr_3$ Layer Thickness on PV Performance. The diffusion length and lifetime of the photogenerated carriers are significantly affected by the thickness of the absorber layer. To optimize the performance of six device structures, the thickness of $CsSnBr_3$ varies from 100 to 1200 nm, as illustrated in Figure 12. As the absorber thickness increases, both the PCE and J_{sc} experience rapid growth until reaching 800 nm. Beyond this point, there is no significant change, indicating saturation in the number of photons available for absorption. Conversely, V_{oc} and FF exhibit a monotonic decrease with the increase in $CsSnBr_3$ layer thickness. This reduction in V_{oc} and FF is attributed to the rise in recombination rate and improved series resistance, respectively. Among the device structures based on TiO_2, PCBM, WS_2, SnO_2, ZnO, and IGZO, the highest PCEs are observed at 19.72, 19.73, 20.02, 19.72, 19.73, and 19.57%, respectively, with an optimal absorber thickness of 800 nm. In the ITO/TiO_2/$CsSnBr_3$/Cu_2O/Au device, an increase in absorber thickness resulted in a decrease in V_{oc}, reducing from 1.33 to 1.22 V. Additionally, J_{sc} exhibited an initial rise from 8.37 to 19.17 mA cm^{-2}, followed by a slight increase to 19.73 mA cm^{-2}. Similarly, the absorber thickness variation led to an initial increase in FF from 83.48 to 84.16%, succeeded by a decrease to 82.37%. Furthermore, PCE demonstrated an increase from 9.27 to 19.72%, with a subsequent further rise to 19.87%. Likewise, devices ITO/PCBM/$CsSnBr_3$/Cu_2O/Au, ITO/WS_2/$CsSnBr_3$/Cu_2O/Au, ITO/SnO_2/$CsSnBr_3$/Cu_2O/

https://doi.org/10.1021/acs.energyfuels.4c00953
Energy Fuels 2024, 38, 8229–8248

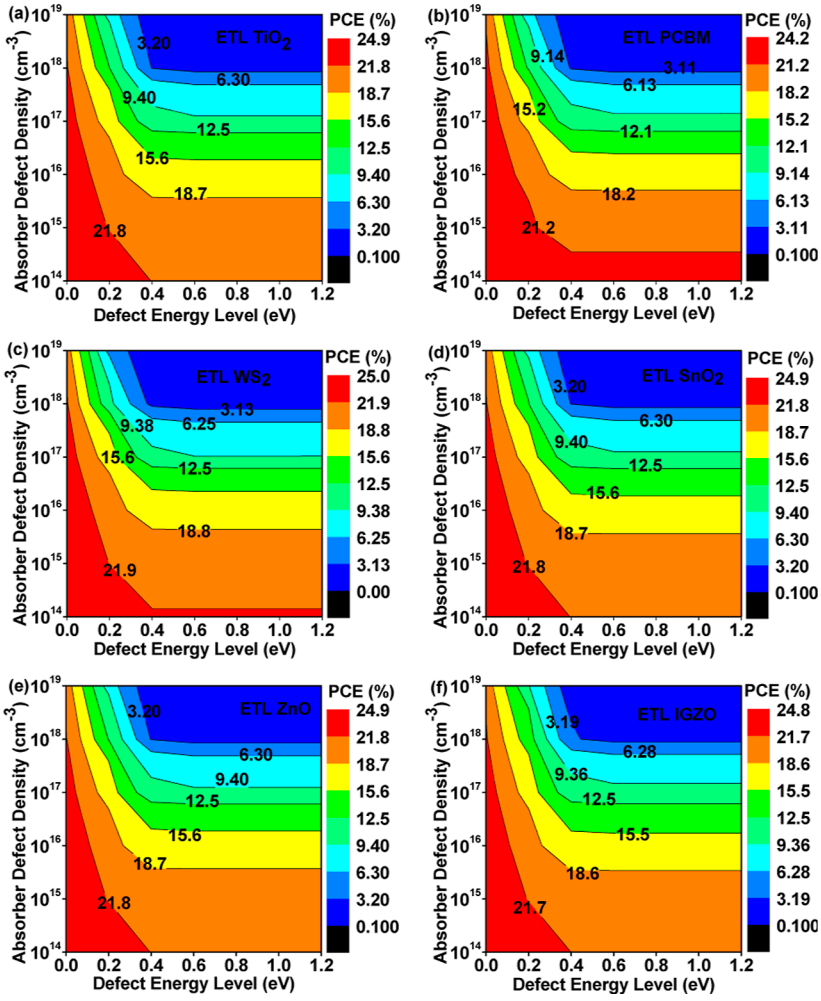

Figure 8. Contour plots depict the influence of defect energy level and absorber defect density on PCEs for different ETLs.

Au, ITO/ZnO/$CsSnBr_3$/Cu_2O/Au, and ITO/IGZO/$CsSnBr_3$/Cu_2O/Au displayed similar trends in PV parameters with an increase in absorber thickness. Since the highest efficiency was achieved at 800 nm, this thickness was deemed optimal for the simulated PSC structures.

3.4.2. Influence of ETL Thickness on PV Performance. Figure 13 illustrates the impact on photovoltaic parameters as the thickness of the ETL varies from 50 to 600 nm, while maintaining constant values for other parameters and setting the absorber thickness at 800 nm. In Figure 13a, it is apparent that an increase in ETL thickness leads to a marginal improvement in PCE for all device structures, except for the PCBM-based PSC, where PCE sharply declines from 19.72 to 9.81%. In Figure 13b, the V_{oc} for all devices remains stable with an increase in ETL thickness, except for the PCBM-based PSC, where V_{oc} decreases from 1.229 to 1.204 V. This trend continues in Figure 13c, where a slight rise in J_{sc} is observed with an increase in ETL thickness. For PCBM- and WS_2-based devices, J_{sc} increases from 19.16 to 19.18 mA/cm^2 and 19.32 to 19.33 mA/cm^2, respectively. In TiO_2-, SnO_2-, ZnO-, and IGZO-based devices, J_{sc} increases from 19.17 to 19.19 mA/cm^2. Figure 13d demonstrates that, with an increase in ETL thickness, TiO_2-, SnO_2-, and ZnO-based devices exhibit negligible changes in FF, while the PCBM-based device sees an increase up to 200 nm, followed by a decrease. WS_2 displays a continuous gradual increase in FF, whereas IGZO shows a continuous gradual decrease in FF with increasing ETL thickness. The optimized thicknesses for TiO_2, PCBM, WS_2, SnO_2, ZnO, and IGZO are determined to be 300, 100, 500, 200, 200, and 200 nm, respectively.

3.4.3. Influence of HTL Thickness on PV Performance. Figure 14 illustrates the impact of varying the thickness of the Cu_2O HTL on PV parameters in $CsSnBr_3$-based PSCs, utilizing TiO_2, PCBM, WS_2, ZnO, SnO_2, and IGZO as ETLs.

Adjusting the HTL thickness is crucial for optimizing performance while minimizing direct contact between the absorber layer and the cathode. Additionally, this layer serves the dual purpose of acting as a capping layer. The focus of our investigation for HTL thickness optimization is solely on Cu_2O since among all HTLs given in Table S1, it demonstrated the highest PCE when used with six different ETLs. Figure 14 reveals that the values of PCE, V_{oc}, J_{sc}, and FF remain consistent for all ETLs as the thickness of Cu_2O (HTL) increases. V_{oc} remains stable at approximately 1.22 V for TiO_2, PCBM, SnO_2, ZnO, and IGZO as ETLs and at around 1.23 V for WS_2 with increased Cu_2O thickness. The J_{sc} value for PCBM shows a lower value of 19.16 mA/cm^2, while WS_2 demonstrates a higher value of 19.32 mA/cm^2 with an increasing Cu_2O thickness. Among all ETLs, WS_2 achieves the highest FF and PCE values at around 84.18 and 20.02%, respectively. On the other hand, the IGZO ETL exhibits the lowest PCE value of about 19.57% with increasing Cu_2O

https://doi.org/10.1021/acs.energyfuels.4c00953
Energy Fuels 2024, 38, 8229−8248

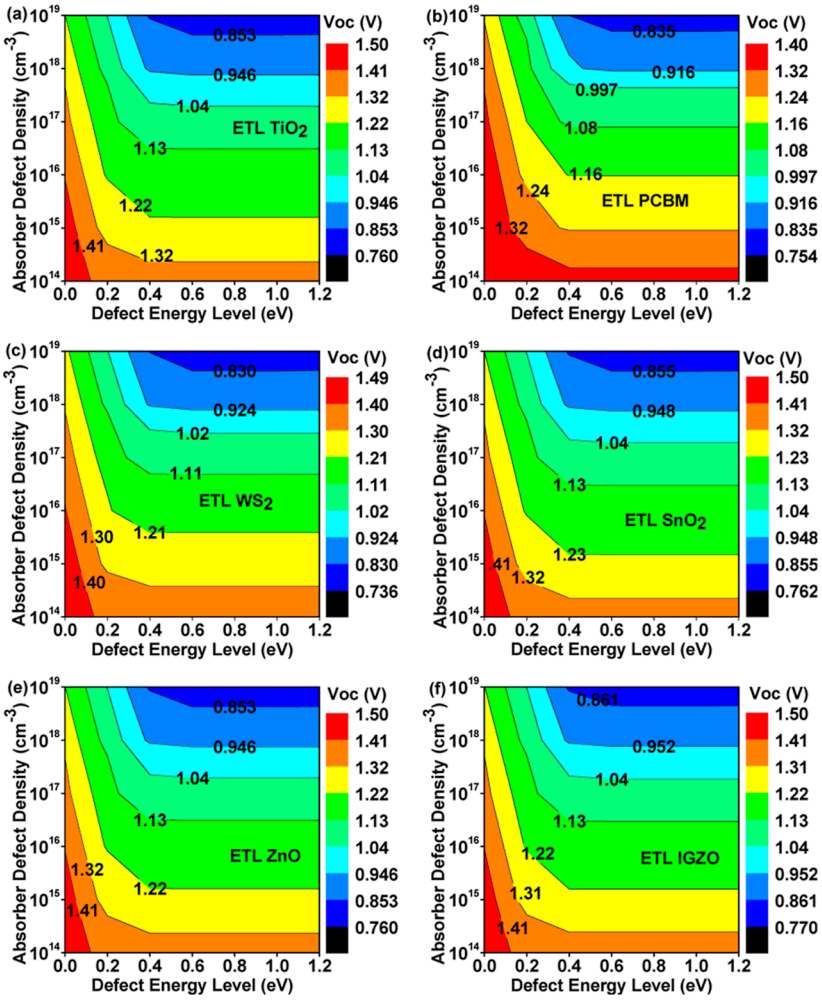

Figure 9. Contour plots depict the influence of defect energy level and absorber defect density on V_{oc} for different ETLs.

thickness. Previous studies have indicated an increase in PCE with an increase in HTL thickness. Typically, a thicker p-type layer is preferred over an n-type layer to reduce the recombination rate, facilitating efficient charge carrier transportation to the respective terminals. However, during the variation of HTL thickness, it is observed that 50 nm is the optimal thickness for achieving higher PCE. Therefore, 50 nm is selected as the optimized HTL thickness for subsequent calculations.

3.5. Influence of the PAL Properties. *3.5.1. Influence of the PAL Acceptor Doping Density.* The acceptor density (N_A) within the perovskite absorber layer (PAL) is a critical parameter influencing PSC performance. Elevating N_A can enhance V_{oc} and efficiency; however, excessive levels may lead to increased recombination and an imbalanced charge distribution. Therefore, finding the optimal balance between N_A and other factors is crucial for achieving maximum efficiency and stability. Additionally, the PSC performance is influenced by the absorbers' electrical behavior, which is itself affected by N_A. N_A was systematically varied from 1×10^{10} to 1×10^{21} cm^{-3} to assess its impact on the PV parameters of the device and determine the optimal N_A for the absorber. Figure 15 depicts the changes in PCE, V_{oc}, J_{sc}, and FF with varying N_A in the absorber for devices with different ETLs. For the ITO/TiO_2/$CsSnBr_3$/Cu_2O/Au device, as shown in Figure 15a, when 1×10^{10} cm^{-3} < N_A < 1×10^{14} cm^{-3}, there is no significant increase in PCE. However, for $N_A > 1 \times 10^{14}$ cm^{-3}, PCE increased from 18.89 to 22.73%. Figure 15b,c exhibits a similar trend, with no substantial changes in V_{oc} and J_{sc} as N_A is varied from 1×10^{10} to 1×10^{14} cm^{-3}. When $N_A > 1 \times 10^{14}$ cm^{-3}, V_{oc} increased from 1.22 to 1.57 V, and J_{sc} decreased from 19.17 to 15.683 mA/cm^2.

Figure 15d indicates that as N_A ranged from 1×10^{10} to 1×10^{15} cm^{-3}, FF increased from 79.8 to 83.66%. For $N_A = 1 \times 10^{16}$ cm^{-3}, FF dropped to 82.45%, but further increases in N_A resulted in elevated FF. Similar performance trends were observed in all other structures. Considering the pursuit of maximum efficiency, the optimum N_A in the PAL was determined as 1×10^{15} cm^{-3} for all ETLs.

3.5.2. Influence of the PAL Defect Density. The defect density (N_t) within the PAL plays a crucial role in influencing the performance of a PSC. Various types of defects in the perovskite material, such as lattice, chemical, or electronic defects, can act as recombination centers for charge carriers, thereby diminishing the overall efficiency of the SC. An increase in N_t within the PAL results in reduced efficiency as higher N_t introduces more recombination centers for charge carriers, leading to a decline in the overall current generated by the cell. Additionally, defects have the capacity to trap charge carriers, thereby reducing the charge carrier lifetime and, consequently, efficiency. Another significant factor impacting the PSC's performance is the long-term stability of the SC.

https://doi.org/10.1021/acs.energyfuels.4c00953
Energy Fuels 2024, 38, 8229−8248

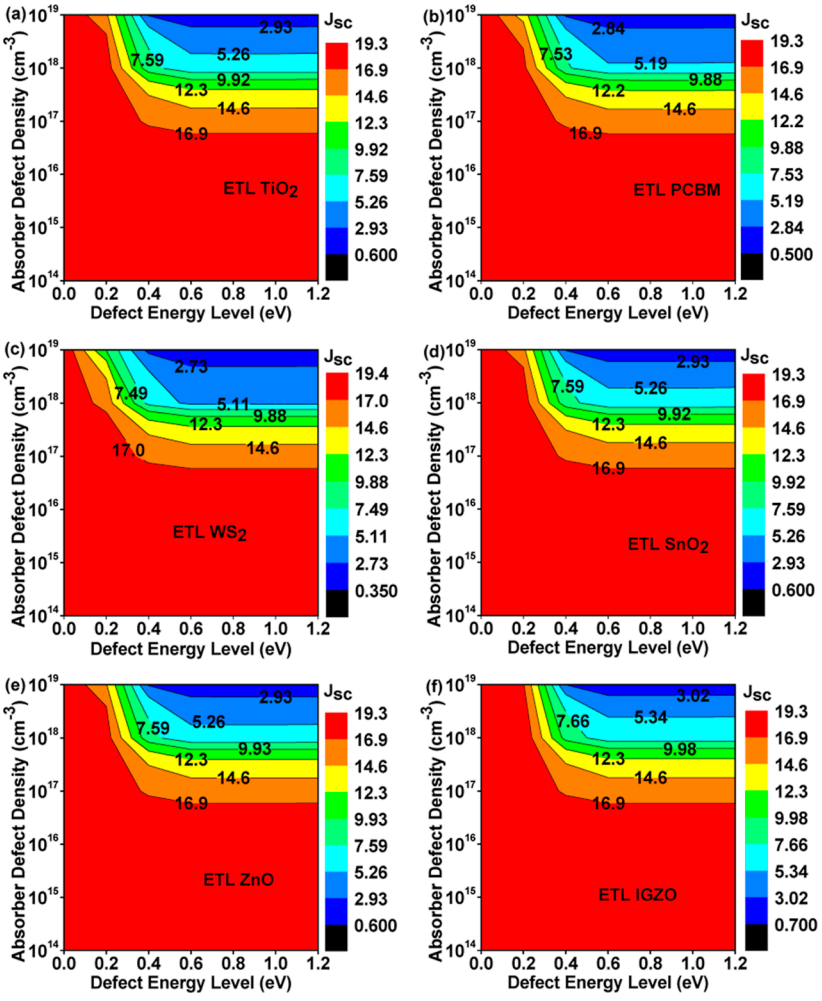

Figure 10. Contour plots depict the influence of defect energy level and absorber defect density on J_{sc} for different ETLs.

Defects can contribute to the instability of the perovskite layer, making it more susceptible to degradation under operational conditions. Therefore, this subsection delves into studying the impact of defect density to provide deeper insights. In Figure 16, the relationship between N_t and PV parameters is illustrated as N_t varies from 1×10^{10} to 1×10^{20} cm^{-3}. Notably, there is no significant change in PV parameters until N_t of the absorber reaches 10^{13} cm^{-3}. Beyond this point, PV parameters show a tendency to decrease from 1×10^{14} cm^{-3} onward. This decline in performance is attributed to SRH nonradiative recombination, defined in eqs 9 and 12, which is a key contributor to device lifetime reduction and carrier recombination.

Figure 16a shows that TiO_2-, PCBM-, WS_2-, SnO_2-, ZnO-, and IGZO-based devices experience a reduction in PCE from 24.84 to 0.013%, 24.13 to 0.011%, 25.01 to 0.008%, 24.84 to 0.013%, 24.84 to 0.013%, and 24.81 to 0.016%, respectively, within the N_t range of 1×10^{10} to 1×10^{20} cm^{-3}. Figure 16b demonstrates a consistent decrease in V_{oc} across all device structures with an increase in N_t. For TiO_2-, PCBM-, WS_2-, SnO_2-, ZnO-, and IGZO-based devices, V_{oc} reduces from 1.54 to 0.63 V, 1.40 to 0.63 V, 1.50 to 0.61 V, 1.54 to 0.63 V, 1.54 to 0.63 V, and 1.51 to 0.64 V, respectively, over the N_t range from 1×10^{10} to 1×10^{20} cm^{-3}. Figure 16c reveals that J_{sc} remains unchanged as $N_t \leq 1 \times 10^{14}$ cm^{-3}. However, once $N_t > 1 \times 10^{14}$ cm^{-3}, J_{sc} significantly decreases for all device configurations. For TiO_2-, PCBM-, WS_2-, SnO_2-, ZnO-, and IGZO-based devices, J_{sc} is reduced from 19.22 to 0.061 mA/cm^2, 19.21 to 0.051 mA/cm^2, 19.37 to 0.038 mA/cm^2, 19.22 to 0.06 mA/cm^2, 19.22 to 0.06 mA/cm^2, and 19.22 to 0.07 mA/cm^2, respectively, within the N_t range of 1×10^{10} to 1×10^{20} cm^{-3}. Figure 16d depicts an increase in FF when N_t is $\leq 1 \times 10^{14}$ cm^{-3} for all structures. For TiO_2-, PCBM-, WS_2-, SnO_2-, ZnO-, and IGZO-based devices, FF increases from 83.87 to 84.94%, 89.58 to 85.13%, 85.89 to 85.03%, 83.90 to 84.94%, 83.79 to 84.95%, and 85.02 to 84.85%, respectively. Beyond $N_t > 1 \times 10^{14}$ cm^{-3}, FF starts to decrease to around 34% for all device structures. In the quest for achieving peak efficiency, the optimal N_t within the PAL was identified as 1×10^{12} cm^{-3} across all ETLs. This comprehensive analysis underscores the critical importance of managing defect density within the absorber layer for optimizing and maintaining the performance and stability of PSCs over time.

3.6. Influence of the ETL Properties. *3.6.1. Influence of the ETL Donor Doping Density (N_D).* The variations in PV parameters, including PCE, V_{oc}, J_{sc}, and FF, in relation to the N_D of TiO_2, PCBM, WS_2, SnO_2, ZnO, and IGZO as ETLs are depicted in Figure 17. The N_D for all ETLs was adjusted within the range of 1×10^{13} to 1×10^{20} cm^{-3}. All PV parameters remained stable when N_D was $\leq 1 \times 10^{16}$ cm^{-3}, and beyond this threshold, a gradual increase in all PV parameters was observed. J_{sc} values for TiO_2, WS_2, ZnO, and IGZO ETLs

https://doi.org/10.1021/acs.energyfuels.4c00953
Energy Fuels 2024, 38, 8229−8248

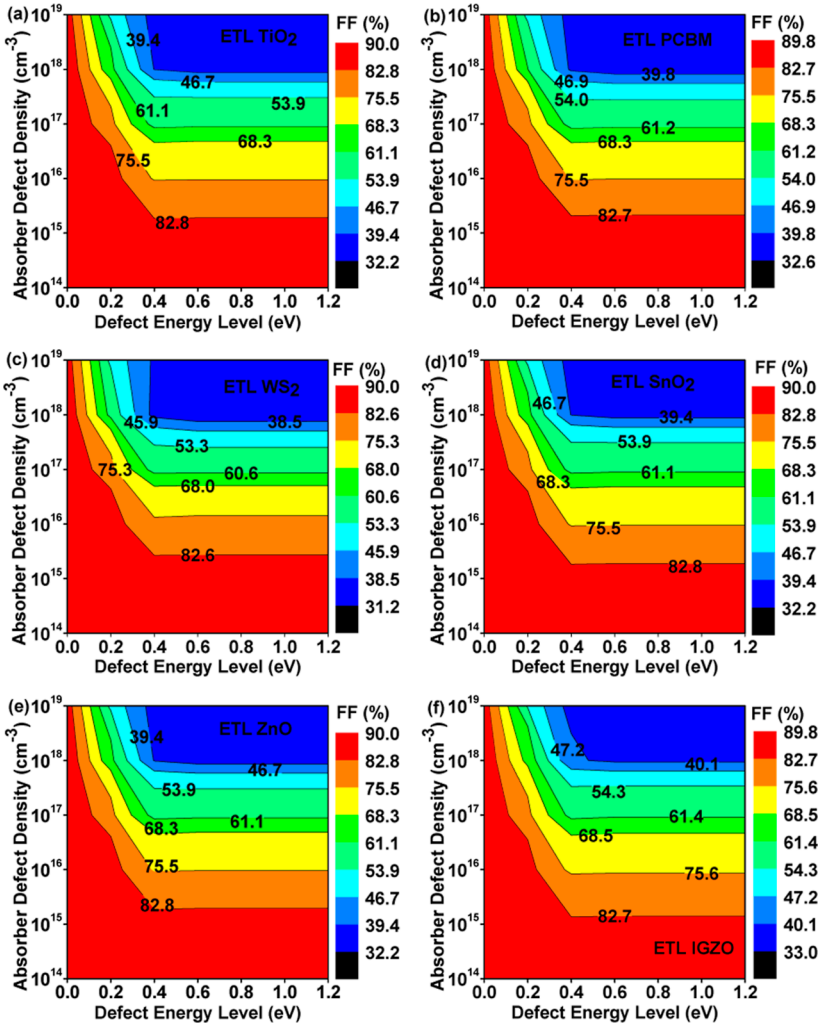

Figure 11. Contour plots depict the influence of defect energy level and absorber defect density on FF for different ETLs.

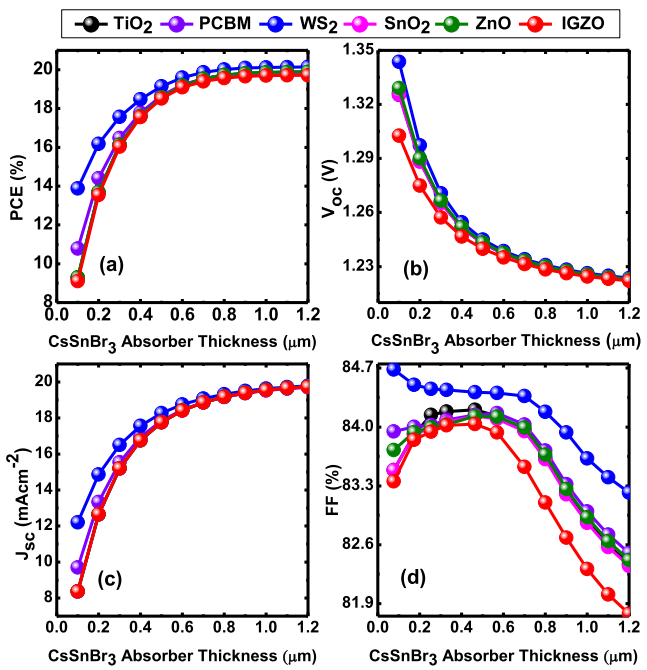

Figure 12. Influence of $CsSnBr_3$ layer thickness on PV performance.

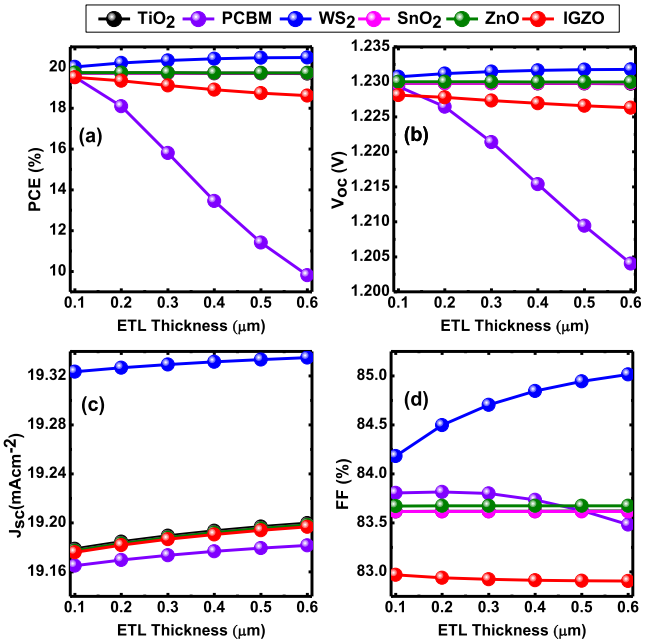

Figure 13. Influence of ETL thickness on PV performance.

https://doi.org/10.1021/acs.energyfuels.4c00953
Energy Fuels 2024, 38, 8229−8248

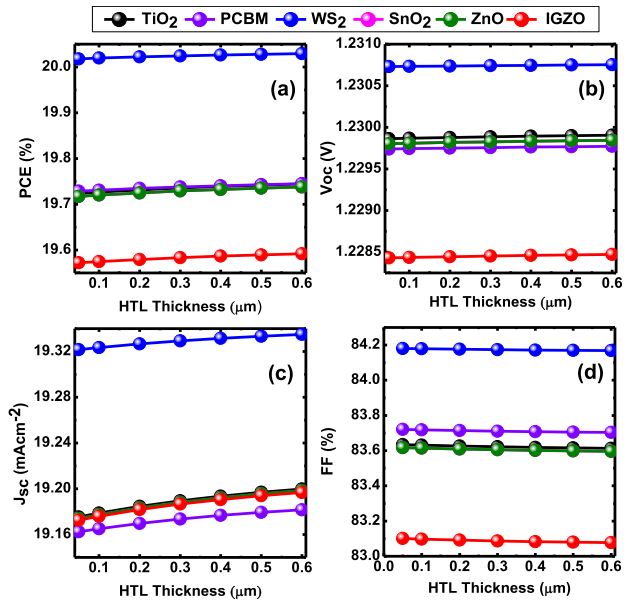

Figure 14. Influence of HTL thickness on PV performance.

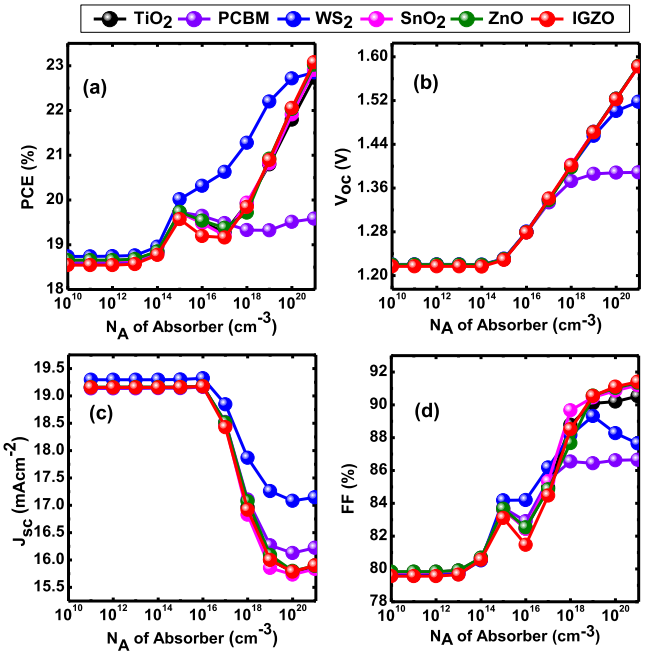

Figure 15. Influence of PAL Acceptor Doping Density on PV performance.

remained constant with varying N_D, while PCBM and SnO_2 exhibited a declining trend as N_D ranged from 1×10^{18} to 1×10^{20} cm^{-3}. For $N_D \geq 1 \times 10^{19}$ cm^{-3}, all PV parameters saturated across all ETLs. The increase in N_D led to an enhancement in PCE, V_{oc}, and FF due to enhanced charge extraction and transportation at the ETL/absorber interfaces. Conversely, lower N_D values resulted in reduced values of these parameters due to increased series resistance. The J_{sc} tends to decrease or remain constant after reaching a certain value of N_D (Figure 17c). The optimum N_D values are 1×10^{18} cm^{-3} for TiO_2, PCBM, WS_2, SnO_2, ZnO, and 1×10^{19} cm^{-3} for IGZO, respectively.

3.6.2. Influence of the ETL Defect Density. Figure 18 depicts the impact of the defect density (N_t) of the ETL on the

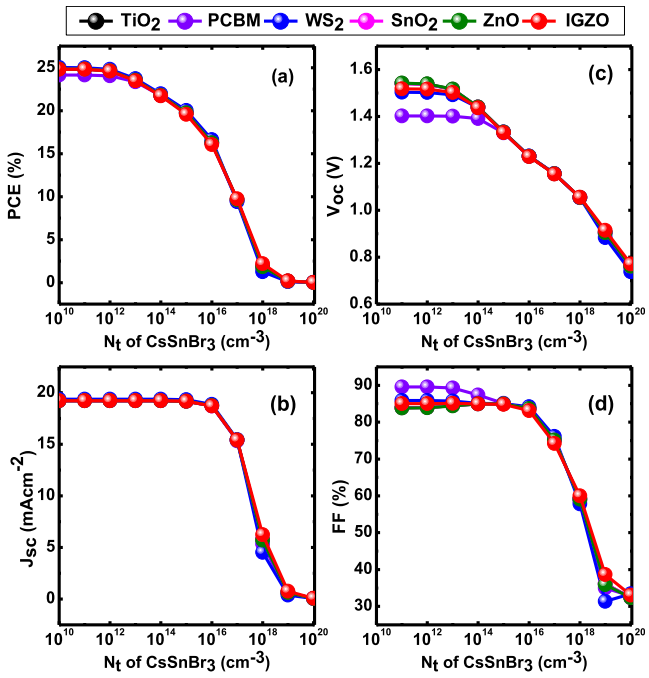

Figure 16. Influence of PAL defect density on PV performance.

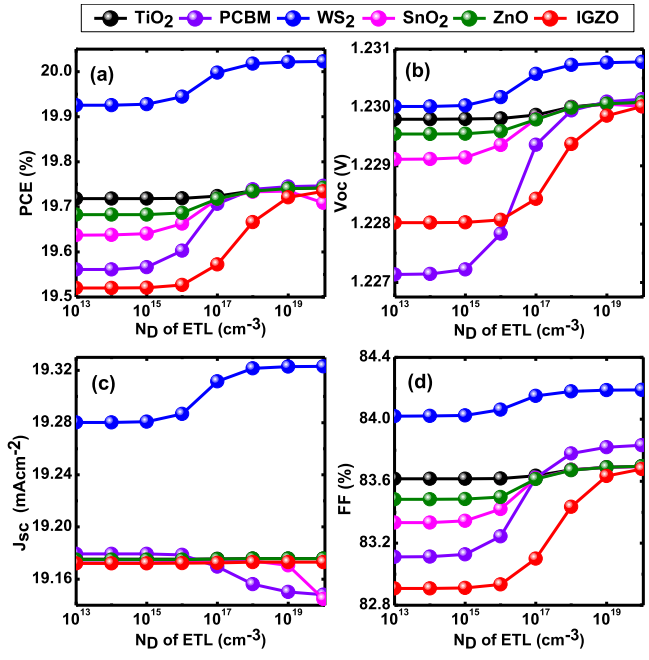

Figure 17. Influence of the ETL donor doping density on PV performance.

PCE, V_{oc}, J_{sc}, and FF. To achieve the targeted N_t for the ETL, the N_t was finetuned within the range of 1×10^{11} to 1×10^{17} cm^{-3}. As illustrated in Figure 18, nearly all performance parameters, PCE, V_{oc}, J_{sc}, and FF, remained constant for all ETLs as the N_t of the ETL increased, except for PCBM, where the PV parameters decreased when N_t surpassed 1×10^{15} cm^{-3}. WS_2 and ZnO, functioning as ETLs, exhibited the highest V_{oc} value at 1.23 V, while other ETLs showed a V_{oc} value of approximately 1.2 V. The FF value for the majority of ETLs remained constant, except for WS_2 and PCBM, which exhibited a slight decrease after reaching 1×10^{15} cm^{-3}. According to the simulated data, the optimized N_t is

https://doi.org/10.1021/acs.energyfuels.4c00953
Energy Fuels 2024, 38, 8229−8248

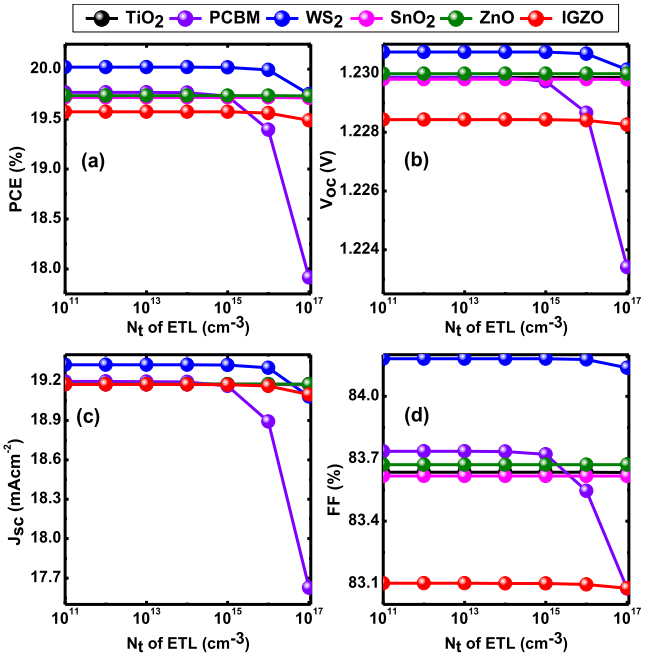

Figure 18. Influence of the ETL defect density on PV performance.

determined to be 1×10^{15} cm^{-3} for all six sets of PSC structures.

3.7. Influence of the HTL Properties. *3.7.1. Influence of the HTL Acceptor Doping Density (N_A).* Figure 19 illustrates

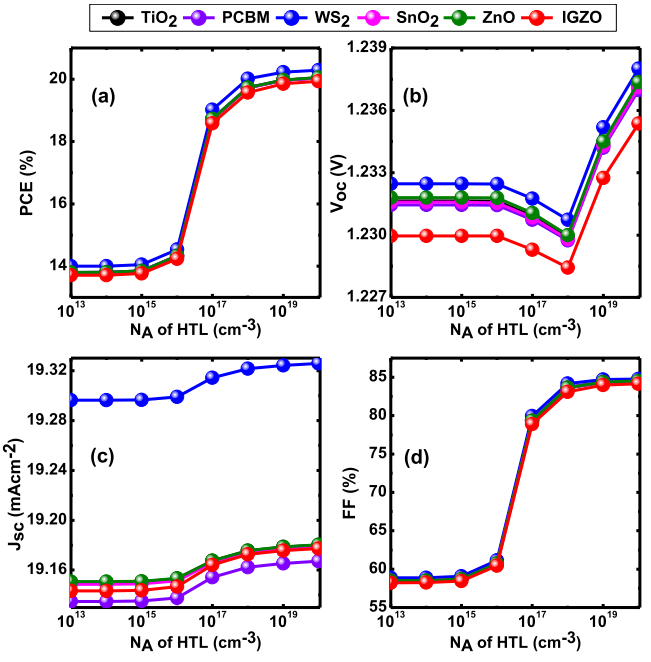

Figure 19. Influence of the HTL acceptor doping density on PV performance.

the variation in PV parameters with an increase in N_A of the HTL for different ETL-based structures. N_A is adjusted within the range of 1×10^{13} to 1×10^{20} cm^{-3} for all device structures under investigation.

In Figure 19a, it is noticeable that PCE values for different ETLs exhibit relatively lower values when $N_A < 1 \times 10^{16}$ cm^{-3} due to a diminished electric field, leading to reduced carrier extraction. Moreover, as N_A exceeds 1×10^{16} cm^{-3}, PCE shows an increasing trend in all device configurations. The PCE of TiO_2, PCBM, WS_2, SnO_2, IGZO, and ZnO increased from 13.79 to 20.04%, 13.8 to 20.03%, 13.99 to 20.28%, 13.78 to 20.03%, 13.8 to 20.05%, and 13.7 to 19.93%, respectively, with the rise in N_A. A similar trend is observed for the FF values in all PSCs (Figure 19d), where FF increases as N_A varies from 1×10^{15} to 1×10^{16} cm^{-3}. Like PCE, the FF of TiO_2, PCBM, WS_2, SnO_2, IGZO, and ZnO increased from 58.48 to 84.47%, 58.56 to 84.51%, 58.86 to 84.78%, 58.47 to 84.46%, 58.50 to 84.49%, and 58.21 to 84.15%, respectively. The J_{sc} values for all ETLs associated with PSCs exhibit a gradual increase with the growing N_A (Figure 19c). The V_{oc} for all device structures rises when N_A is $\leq 1 \times 10^{15}$ cm^{-3}, and when 1×10^{15} $cm^{-3} < N_A < 1 \times 10^{17}$, V_{oc} decreases. For $N_A > 1 \times 10^{19}$ cm^{-3}, V_{oc} again increases as the N_A rises from 1×10^{15} to 1×10^{17} cm^{-3}. The optimum N_A is found to be 1×10^{19} cm^{-3} for all ETL-based devices.

3.7.2. Influence of the HTL Defect Density. The defect density (N_t) of the HTL ranges from 1×10^{11} to 1×10^{17} cm^{-3}, as illustrated in Figure 20. The PV parameters of various

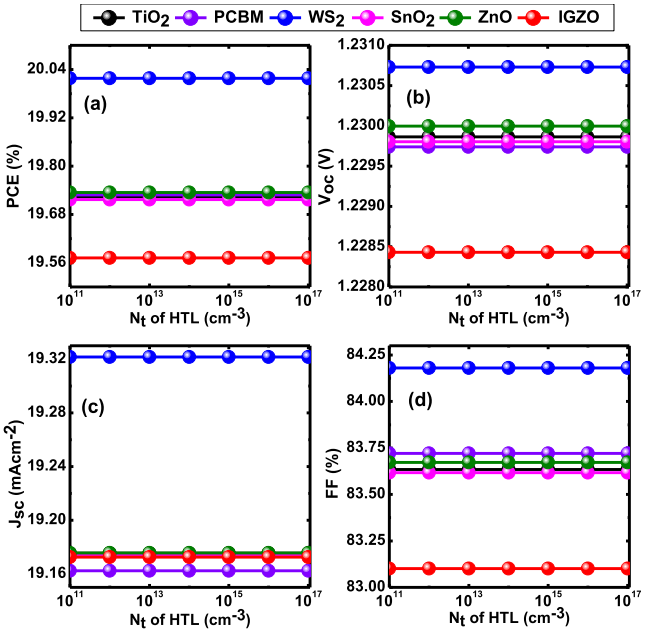

Figure 20. Influence of the HTL defect density on PV performance.

ETLs remained constant as the N_t of the HTL increased to 1×10^{17} cm^{-3}. Consequently, the performance of six sets of $CsSnBr_3$-based PSCs exhibited an insignificant impact with the increasing N_t. The FF displayed a similar trend to the PCE for all ETLs as the N_t of the HTL is varied. The V_{oc} and J_{sc} values remained constant across all ETL device configurations as the N_t of the HTL increased. Therefore, the increase in N_t had an insignificant effect on the device configurations. The optimized value for N_t is established at 1×10^{15} cm^{-3} for all the six device structures for further enhancement.

3.8. Influence of Interface Properties. *3.8.1. Influence of $CsSnBr_3$/ETL Interface Defect Density on PV Performance.* Figure 21 depicts the alterations in PCE, V_{oc}, J_{sc}, and FF in relation to the varying $CsSnBr_3$/ETL interface defect density (N_t). To observe the fluctuations in these PV parameters, the N_t value was adjusted from 1×10^{10} to 1×10^{20} cm^{-2}. When N_t is $\leq 1 \times 10^{13}$ cm^{-2}, all PV parameters remain stable;

https://doi.org/10.1021/acs.energyfuels.4c00953
Energy Fuels 2024, 38, 8229−8248

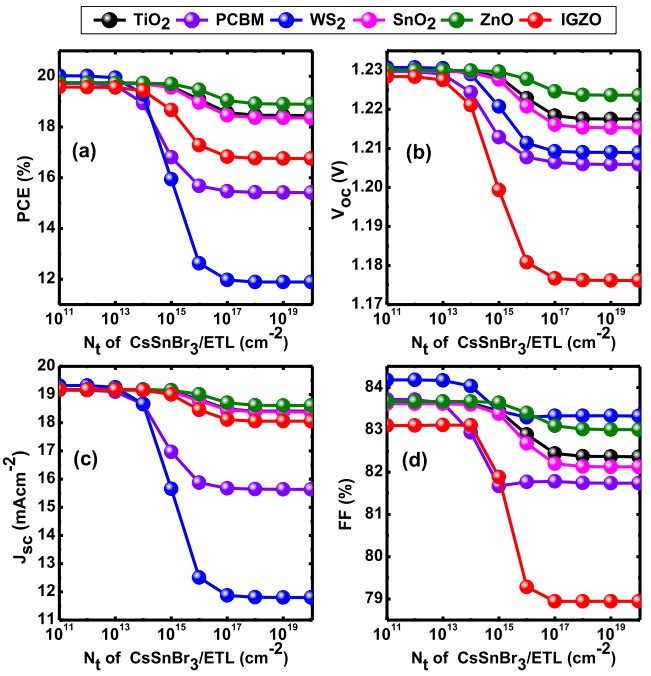

Figure 21. Influence of $CsSnBr_3$/ETL interface defect density on PV performance.

however, surpassing 1×10^{13} cm^{-2}, all PV parameters commence a decline. The PCE of TiO_2, PCBM, WS_2, SnO_2, IGZO, and ZnO decreases from 19.72 to 18.45%, 19.72 to 15.41%, 20.01 to 11.88%, 19.71 to 18.34%, 19.73 to 18.90%, and 19.57 to 16.76%, respectively, with an increase in N_t of the $CsSnBr_3$/ETL interface. The V_{oc} of TiO_2, PCBM, WS_2, SnO_2, IGZO, and ZnO also decreases from 1.229 to 1.217 V, 1.229 to 1.205 V, 1.23 to 1.208 V, 1.229 V to 1.215 V, 1.23 to 1.223 V, and 1.228 to 1.176 V, respectively, as the N_t of the $CsSnBr_3$/ETL interface increases. The limit on V_{oc} imposed by recombination at the interface is determined by eq 15 as[42]

$$V_{oc} = \frac{\phi_B}{q} - \frac{\eta KT}{q} \ln\left(\frac{qN_v S_{it}}{J_{sc}}\right) \quad (15)$$

where S_{it} is the interface recombination velocity and ϕ_B is the effective barrier height. Equation 15 reveals that high N_t will generate S_{it} leading to a decrease in V_{oc}. To achieve high values of V_{oc}, it is desirable to maximize the effective barrier height at the $CsSnBr_3$/ETL interface, preventing the recombination of charge carriers.

The J_{sc} of TiO_2, PCBM, WS_2, SnO_2, IGZO, and ZnO decreases from 19.17 to 18.40%, 19.16 to 15.63%, 19.32 to 11.79%, 19.17 to 18.38%, 19.17 to 18.60%, and 19.17 to 18.05%, respectively, with an increase in the N_t of the $CsSnBr_3$/ETL interface. Among all ETLs, WS_2 PV performance is significantly impacted with an increase in N_t. The FF of all ETL-based devices decreases with an increase in N_t of the $CsSnBr_3$/ETL interface (Figure 21d). The simulation results highlight that the optimal N_t for device simulation is 1×10^{13} cm^{-2}.

3.8.2. Influence of Cu_2O/$CsSnBr_3$ Interface Defect Density on PV Performance. Numerous defect states commonly coexist at the interface between the absorber and charge transport layers, and the performance of the PSC is significantly influenced by the quality of this interface. Previous research indicates that the N_t on the irradiation side has a more pronounced impact on PV performance compared to the N_t at the rear interface.[43] Figure 22 depicts the variations in PV cell

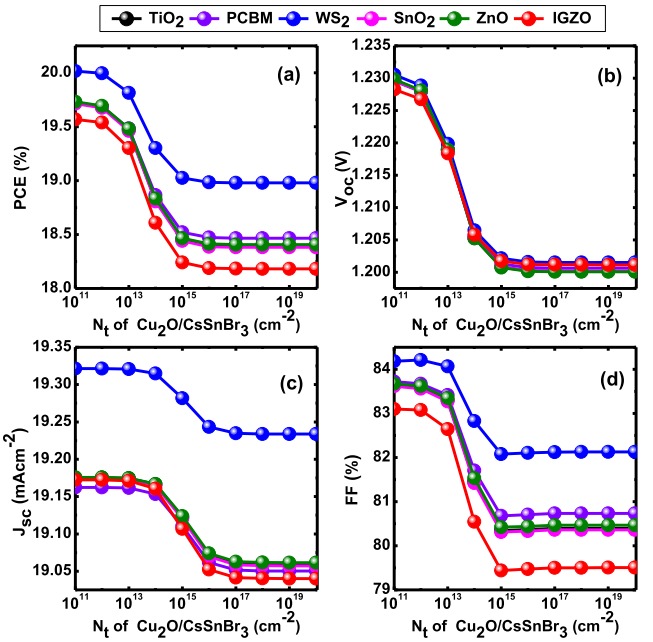

Figure 22. Influence of Cu_2O/$CsSnBr_3$ interface defect density on PV performance.

parameters, including PCE, V_{oc}, J_{sc}, and FF, in relation to the varying N_t at the Cu_2O/$CsSnBr_3$ interface. All PV parameters exhibit a decreasing trend as the N_t is varied from 1×10^{11} to 1×10^{20} cm^{-2}. When N_t is $\leq 1 \times 10^{13}$ cm^{-2}, all PV parameters remain stable; however, beyond 1×10^{13} cm^{-2}, a decline is observed in all parameters. Simulation data reveals that an increase in N_t leads to a rise in recombination rate and a decrease in PCE. Higher N_t at the Cu_2O/$CsSnBr_3$ interface results in increased trap and recombination centers, thereby diminishing PSC performance. The simulation results highlight that the optimal N_t for device simulation is 1×10^{13} cm^{-2}.

3.9. Influence of Capacitance (*C*–*V*) and Mott–Schottky (M–S) Analysis on PV Performance. The Mott–Schottky (M–S) analysis serves as a valuable tool for comprehending the electrical properties of semiconductor materials and provides insights into the behavior of PSCs. This method is widely recognized and reliable, specifically for evaluating the built-in potential (V_{bi}) and elucidating the operational functions and doping levels of an electrode.[24,31] In the M–S plot, the V_{bi} is typically represented by the x-axis intercept, while the slope can estimate the doping density of the absorber layer. In all the investigated PSC structures, V_{bi} was determined to be 1.3 V through the extrapolation of the x-intercept on the M–S plot. Figure 23 illustrates the M–S plot for the device, considering six distinct ETLs. It is evident that all of them display a negative slope, indicating the p-type conductivity of the device.[44] A higher flat band potential results in a reduced energy barrier for carrier transfer at the interface. Consequently, a lower voltage is needed to facilitate the transportation of charge carriers across the interface.[45] In simpler terms, a device with the greatest V_{bi} will yield the highest V_{oc}. These findings align with the simulated performance results of the device using various ETLs. Equation 16 gives the depletion capacitance per unit area as

https://doi.org/10.1021/acs.energyfuels.4c00953
Energy Fuels 2024, 38, 8229–8248

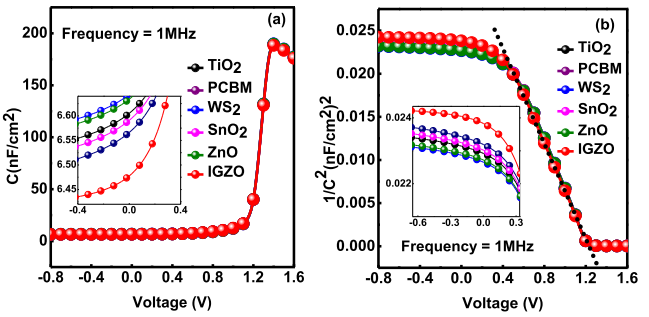

Figure 23. C−V and M−S plot for six optimized structures.

$$\frac{1}{C_j^2} = \frac{2}{q\varepsilon_s\varepsilon_0 N_D}(V_{bi} - V) \tag{16}$$

Accordingly, if the slope of M−S plot is

$$\text{slope} = \frac{\partial}{\partial V}\left(\frac{1}{C_j^2}\right) \tag{17}$$

Then, the value of N_D follows from

$$N_D = \frac{2}{q\varepsilon_s\varepsilon_0}\frac{-1}{\text{slope}} \tag{18}$$

This study explores the variation of capacitance and M−S concerning applied voltage in six optimized PSC device structures. These structures utilize Cu_2O as the HTL and TiO_2, PCBM, WS_2, SnO_2, ZnO, and IGZO as the corresponding ETLs, with $CsSnBr_3$ serving as the absorber layer. Figure 23a illustrates a nonlinear increase in capacitance with applied voltage, while Figure 23b shows a noticeable decrease in the M−S plot as the voltage increases. This phenomenon can be attributed to several influential factors. First, variations in voltage induce changes in charge carrier density, thereby initiating adjustments in capacitance. Additionally, the influence of defect states emerges as a crucial determinant in capacitance dynamics, with voltage fluctuations leading to shifts in the occupancy and behavior of these states. The impact of electric field effects is noteworthy, as the increased applied voltage establishes a more robust electric field, affecting charge distribution and contributing to the observed alterations in capacitance. Furthermore, the broadening of the depletion region at the semiconductor surface with increasing voltage serves as an additional contributing factor, playing a pivotal role in shaping the overall capacitance dynamics. PSCs utilizing TiO_2, PCBM, WS_2, SnO_2, ZnO, and IGZO exhibited the maximum capacitance values, measuring 189.79, 189.57, 190.22, 189.76, 189.92, and 188.53 nF/cm^2, respectively. Among these, the WS_2-based PSC exhibited the highest capacitance, while the IGZO-based PSC showed lowest capacitance value as the voltage increase.

3.10. *J*−*V* and QE Characteristics. Figure 24a,b illustrates the before and after optimization stages of the *J*−*V* curve for six considered PSCs. Before optimization, PCBM demonstrated a J_{sc} of 19.16 mA cm^{-2}, WS_2 exhibited 19.32 mA cm^{-2}, while all other devices relying on ETLs displayed a J_{sc} of 19.17 mA cm^{-2}. The V_{oc} for WS_2 and ZnO was 1.23 V, whereas for all other devices, it stood at 1.22 V. In contrast, during the final optimization, the J_{sc} for TiO_2 decreased to 18.96 mA cm^{-2}, while that for IGZO remained constant. PCBM, WS_2, SnO_2, and ZnO showcased improved J_{sc} values of 19.21, 19.6, 19.22,

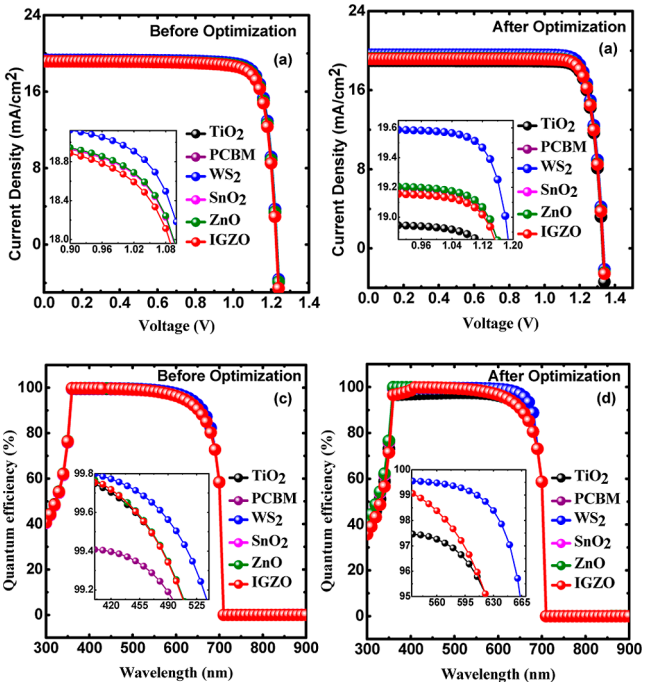

Figure 24. Before and after optimization stages of the (a,b) *J*−*V* curve and (c,d) QE curves.

and 19.22 mA cm^{-2}, respectively. Following the final optimization process, all ETL-based devices exhibited a V_{oc} of approximately 1.33 V. Figure 24c,d depicts the variation of QE concerning the wavelength for $CsSnBr_3$-based PSCs during both before and after optimization process. The QE, representing the proportion of charge carriers generated by a SC to incident photons, is influenced by the light wavelength. The QE typically improves as the absorber thickness increases, allowing for greater photon absorption. Observations indicate that QE remains nearly constant in the wavelength range of 360−600 nm and decreases beyond this range under both initial and final optimized conditions. Figure 24c demonstrates that under initial (before) optimization conditions, the QE is almost 100% for all six structures at a wavelength of about 360 nm. After final optimization condition, PSCs based on ITO/ETL/$CsSnBr_3$/Cu_2O/Au exhibit a modest decline in QE values in comparison to the before optimization, as can be seen in Figure 24d, suggesting a negligible loss in QE. The bandgap of the light-harvesting layer ($E_{g(CsSnBr_3)}$ = 1.75 eV) is aligned with the initial and final optimization curves, where no device structure (out of six) shows QE beyond 700 nm.[44]

3.11. Comparative Study between SCAPS-1D and wxAMPS Results. To enhance the robustness and credibility assessment of the results obtained from the SCAPS-1D simulator, we conducted additional evaluations using simulations performed with the wxAMPS program. Table 3 provides a comprehensive overview of the PV parameters for six different structures of $CsSnBr_3$-based devices. For the TiO_2-based PSC, the SCAPS-1D simulator yields a PCE of 21.64%, whereas the wxAMPS simulator records a PCE of 20.60%. Similarly, employing PCBM as the ETL results in a PCE of 21.94% in SCAPS-1D, while the wxAMPS simulator shows a PCE of 20.42%. The WS_2-based PSC demonstrates a PCE of 22.43% in SCAPS-1D, and a slightly lower PCE of 21.85% in the wxAMPS simulator. Furthermore, employing SnO_2, ZnO, and IGZO as ETLs in $CsSnBr_3$-based PSCs results in PCE

https://doi.org/10.1021/acs.energyfuels.4c00953
Energy Fuels 2024, 38, 8229−8248

Table 3. Comparative Study between SCAPS-1D and wxAMPS Results

device structure	software	PCE (%)	V_{OC} (V)	J_{SC} (mA cm^{-2})	FF (%)
ITO/TiO_2/$CsSnBr_3$/Cu_2O/Au	SCAPS-1D	21.64	1.33	18.96	85.78
	wxAMPS	20.60	1.23	19.95	83.92
ITO/PCBM/$CsSnBr_3$/Cu_2O/Au	SCAPS-1D	21.94	1.33	19.22	85.65
	wxAMPS	20.42	1.23	19.67	84.37
ITO/WS_2/$CsSnBr_3$/Cu_2O/Au	SCAPS-1D	22.43	1.33	19.59	85.80
	wxAMPS	21.85	1.24	20.35	86.58
ITO/SnO_2/$CsSnBr_3$/Cu_2O/Au	SCAPS-1D	21.94	1.33	19.22	85.65
	wxAMPS	20.68	1.23	19.68	85.41
ITO/ZnO/$CsSnBr_3$/Cu_2O/Au	SCAPS-1D	21.94	1.33	19.22	85.65
	wxAMPS	20.37	1.24	19.34	84.93
ITO/IGZO/$CsSnBr_3$/Cu_2O/Au	SCAPS-1D	21.88	1.33	19.17	85.65
	wxAMPS	20.14	1.23	19.38	84.47

values of 21.94, 21.94, and 21.88%, respectively, in the SCAPS-1D simulator. Conversely, the wxAMPS simulator shows slightly reduced PCE values of 20.68, 20.37, and 20.14% for SnO_2, ZnO, and IGZO, respectively. Concerning the V_{oc}, for TiO_2-based structure, the SCAPS-1D simulator indicates a V_{oc} of 1.33 V, while the wxAMPS simulator records a slightly lower value of 1.23 V. Both simulators consistently exhibit almost similar patterns of results for V_{oc} across all device configurations. Comparing the PV parameters of the six PSC structures reveals that SCAPS-1D and wxAMPS simulators yield nearly identical results, except for PCE and FF, where wxAMPS exhibits slightly lower values than SCAPS-1D. The results obtained from both simulators contribute valuable insights into the charge transport materials and absorber material suitable for optimal device configuration. The consistent agreement between the two simulators for all six sets of optimum device configurations enhances the reliability of the presented results for further investigation. Minor discrepancies in simulation results between SCAPS-1D and wxAMPS can be primarily ascribed to variations in numerical algorithms, models, grid resolution, meshing, boundary conditions, simulation settings, convergence criteria, and software implementation. These diverse elements collectively contribute significantly to the observed differences in outcomes generated by the two simulators.

3.12. Comparative Study of SCAPS-1D Results with Prior Research Work. Among the 70 structures considered, we focused on further investigating and optimizing the performance of the top six structures with the following architectures: ITO/TiO_2/$CsSnBr_3$/Cu_2O/Au, ITO/PCBM/$CsSnBr_3$/Cu_2O/Au, ITO/WS_2/$CsSnBr_3$/Cu_2O/Au, ITO/SnO_2/$CsSnBr_3$/Cu_2O/Au, ITO/ZnO/$CsSnBr_3$/Cu_2O/Au, and ITO/IGZO/$CsSnBr_3$/Cu_2O/Au. The outcomes of this optimization study are outlined in Table 4, providing a basis for a comprehensive and equitable comparison. Table 5 provides a comparative analysis of the PV parameters for the six presented device configurations with recently published optimal configurations. The ITO/TiO_2/$CsSnBr_3$/Spiro-OMeTAD/Au heterostructure has been documented with the highest experimental PCE at 10.46%. Simulation has previously yielded the highest PCE of 17.94%. This study presents, for the first time, a record-breaking PCE >22% for the device structure employing $CsSnBr_3$ as the absorber layer.

Table 4. Optimization Parameters: Thickness, N_A (cm^{-3}), N_D (cm^{-3}), and N_t (cm^{-3}) of the HTL (Cu_2O), Absorber Layer $CsSnBr_3$, and Different ETLs

set	layers	thickness (μm)	acceptor density, N_A (cm^{-3})	donor density, N_D (cm^{-3})	defect density, N_t (cm^{-3})
set-1	TiO_2	0.3	1×10^{19}	1×10^{18}	1×10^{14}
	Cu_2O	0.05	1×10^{15}		1×10^{15}
	$CsSnBr_3$	0.8			1×10^{14}
set-2	PCBM	0.1	1×10^{19}	1×10^{18}	1×10^{14}
	Cu_2O	0.05	1×10^{15}		1×10^{15}
	$CsSnBr_3$	0.8			1×10^{14}
set-3	WS_2	0.5	1×10^{19}	1×10^{18}	1×10^{14}
	Cu_2O	0.05	1×10^{15}		1×10^{15}
	$CsSnBr_3$	0.8			1×10^{14}
set-4	SnO_2	0.1	1×10^{19}	1×10^{18}	1×10^{14}
	Cu_2O	0.05	1×10^{15}		1×10^{15}
	$CsSnBr_3$	0.8			1×10^{14}
set-5	ZnO	0.1	1×10^{19}	1×10^{18}	1×10^{14}
	Cu_2O	0.05	1×10^{15}		1×10^{15}
	$CsSnBr_3$	0.8			1×10^{14}
set-6	IGZO	0.1	1×10^{19}	1×10^{19}	1×10^{14}
	Cu_2O	0.05	1×10^{15}		1×10^{15}
	$CsSnBr_3$	0.8			1×10^{14}

4. CONCLUSIONS

SCAPS-1D simulations were utilized to systematically improve the PV characteristics of Pb-free $CsSnBr_3$ PSCs, and the key findings are summarized as follows:

Optimal PCEs were identified through simultaneous adjustments to the absorber layer thickness and defect density (N_t). The most favorable PCEs were attained with absorber thickness in the range of 0.6−1.2 μm and N_t set at 1×10^{13} cm^{-3}. In the case of PCBM, the lowest and highest PCEs were observed with WS_2. Meanwhile, varying the defect energy level (E_t) alongside N_t revealed that the best PCEs occurred with defect densities ranging from 1×10^{14} to 1×10^{16} cm^{-3} and E_t set at 0.2 eV. The PV characteristics are significantly influenced by the $CsSnBr_3$ thickness and ETLs, while the Cu_2O thickness has a negligible effect. Doping densities in the $CsSnBr_3$ layer, ETL, and Cu_2O (HTL) significantly influence the PV performance. The N_t of the charge transport materials also has a significant effect on the PV parameters except for HTL. The dopant density in the CTM affects the PSC performance. PV parameters deteriorate as the N_t at the $CsSnBr_3$/ETL and HTL/$CsSnBr_3$ interfaces increases. The optimal N_t for both interfaces were found to be 1×10^{13} cm^{-3} for the best PSC

https://doi.org/10.1021/acs.energyfuels.4c00953
Energy Fuels 2024, 38, 8229−8248

Table 5. Comparative Study of SCAPS-1D Results with Prior Research Work[a]

type	device structure	PCE (%)	V_{oc} (V)	J_{sc} (mA cm^{-2})	FF (%)	year	ref
E	FTO/TiO_2/$CsSnBr_3$/Spiro-OMeTAD/Au	0.10	0.19	1.57	34	2015	27
E	FTO/TiO_2/$CsSnBr_3$:SnF_2/Spiro-OMeTAD/Au	0.95	0.41	3.99	58	2015	27
E	FTO/TiO_2/$CsSnBr_3$:SnF_2/Spiro-OMeTAD/Au	2.04	0.4	9.1	56	2016	11
E	FTO/TiO_2/$CsSnBr_3$/Spiro-OMeTAD/Au	0.01	0.1	0.4	38	2016	11
E	ITO/TiO_2/$CsSnBr_3$/Spiro-OMeTAD/Au	10.46	0.85	21.23	58	2016	33
E	ITO/MoO_3/$CsSnBr_3$:SnF_2/C_{60}/BCP/Ag	0.5	0.45	2.1	52	2016	16
E	ITO/MoO_3/$CsSnBr_3$:SnF_2/C_{60}/BCP/Ag	0.55	0.407	2.4	55	2016	16
E	ITO/MoO_3/$CsSnBr_3$:SnF_2/C_{60}/BCP/Ag	0.26	0.41	1.6	38	2016	16
E	FTO/TiO_2/$CsSnBr_3$/MoO_3 (20 nm)/Al	0.05	0.08	2.60	25	2021	21
E	FTO/TiO_2/$CsSnBr_3$/MoO_3 (30 nm)//Al	1.5	0.38	11.96	34	2021	21
E	FTO/TiO_2/$CsSnBr_3$/MoO_3 (40 nm)/Al	0.58	0.28	5.86	35	2021	21
T	FTO/SnO_2/$CsSnBr_3$/CuI/Au	17.06	1.19	16.94	84.19	2023	46
T	FTO/TiO_2/$CsSnBr_3$/P3HT/Au	17.94	1.3	18	74.5	2023	24
T	ITO/TiO_2/$CsSnBr_3$/Cu_2O/Au	21.64	1.330	18.96	85.78		b
T	ITO/PCBM/$CsSnBr_3$/Cu_2O/Au	21.94	1.332	19.22	85.65		b
T	ITO/WS_2/$CsSnBr_3$/Cu_2O/Au	22.43	1.333	19.59	85.80		b
T	ITO/SnO_2/$CsSnBr_3$/Cu_2O/Au	21.94	1.332	19.22	85.65		b
T	ITO/ZnO/$CsSnBr_3$/Cu_2O/Au	21.94	1.332	19.22	85.65		b
T	ITO/IGZO/$CsSnBr_3$/Cu_2O/Au	21.88	1.332	19.17	85.65		b

[a]E—experimental, T—theoretical. [b]This work.

performance. The optimized ITO/WS_2/$CsSnBr_3$/Cu_2O/Au device structure achieved the highest PCE of 22.43%, V_{oc} of 1.33 V, J_{sc} of 19.59 mA/cm^2, and FF of 85.80%. The PCBM-, SnO_2-, ZnO-based devices showed a PCE of 21.94%. Meanwhile, TiO_2- and IGZO-based devices exhibited PCEs of 21.64 and 21.88%. Additionally, the simulated outcomes generated by SCAPS-1D were replicated and confirmed through validation using the wxAMPS device simulator.

■ ASSOCIATED CONTENT

Supporting Information

The Supporting Information is available free of charge at https://pubs.acs.org/doi/10.1021/acs.energyfuels.4c00953.

Material parameters of different HTLs used in the simulation and performance of 70 different configurations with additional supplementary results (PDF)

■ AUTHOR INFORMATION

Corresponding Author

Brajendra Singh Sengar − *Department of Electronics and Communication Engineering, National Institute of Technology, Srinagar 190006, India;* orcid.org/0000-0001-6993-1311; Email: brajendra.singh@nitsri.ac.in

Author

Shazia Akhtar Dar − *Department of Electronics and Communication Engineering, National Institute of Technology, Srinagar 190006, India*

Complete contact information is available at: https://pubs.acs.org/10.1021/acs.energyfuels.4c00953

Notes

The authors declare no competing financial interest.

■ ACKNOWLEDGMENTS

The authors express their sincere gratitude to Marc Burgelman and his colleagues at the University of Gent, Belgium for supplying the SCAPS simulation package. They would also like to thank Professor Fonash from Penn State University for providing the wxAMPS simulation package.

■ REFERENCES

(1) Kojima, A.; Teshima, K.; Shirai, Y.; Miyasaka, T. Organometal Halide Perovskites as Visible-Light Sensitizers for Photovoltaic Cells. *J. Am. Chem. Soc.* **2009**, *131* (17), 6050−6051.

(2) Park, J.; Kim, J.; Yun, H.-S.; Paik, M. J.; Noh, E.; Mun, H. J.; Kim, M. G.; Shin, T. J.; Seok, S., II Controlled Growth of Perovskite Layers with Volatile Alkylammonium Chlorides. *Nature* **2023**, *616* (7958), 724−730.

(3) Chowdhury, T. A.; Bin Zafar, M. A.; Sajjad-Ul Islam, Md.; Shahinuzzaman, M.; Islam, M. A.; Khandaker, M. U. Stability of Perovskite Solar Cells: Issues and Prospects. *RSC Adv.* **2023**, *13* (3), 1787−1810.

(4) Mazumdar, S.; Zhao, Y.; Zhang, X. Stability of Perovskite Solar Cells: Degradation Mechanisms and Remedies. *Front. Electron.* **2021**, *2*, 712785.

(5) Dipta, S. S.; Uddin, A. Stability Issues of Perovskite Solar Cells: A Critical Review. *Energy Technol.* **2021**, *9* (11), 2100560.

(6) Babayigit, A.; Ethirajan, A.; Muller, M.; Conings, B. Toxicity of Organometal Halide Perovskite Solar Cells. *Nat. Mater.* **2016**, *15* (3), 247−251.

(7) Babayigit, A.; Duy Thanh, D.; Ethirajan, A.; Manca, J.; Muller, M.; Boyen, H.-G.; Conings, B. Assessing the toxicity of Pb- and Sn-based perovskite solar cells in model organism Danio rerio. *Sci. Rep.* **2016**, *6* (1), 18721.

(8) Ren, M.; Qian, X.; Chen, Y.; Wang, T.; Zhao, Y. Potential Lead Toxicity and Leakage Issues on Lead Halide Perovskite Photovoltaics. *J. Hazard. Mater.* **2022**, *426*, 127848.

(9) Behrouznejad, F.; Shahbazi, S.; Taghavinia, N.; Wu, H.-P.; Wei-Guang Diau, E. A Study on Utilizing Different Metals as the Back Contact of CH3NH3PbI3 Perovskite Solar Cells. *J. Mater. Chem. A* **2016**, *4* (35), 13488−13498.

(10) Bing, J.; Kim, J.; Zhang, M.; Zheng, J.; Lee, D. S.; Cho, Y.; Deng, X.; Lau, C. F. J.; Li, Y.; Green, M. A.; Huang, S.; Ho-Baillie, A. W. Y. The Impact of a Dynamic Two-Step Solution Process on Film Formation of Cs0.15(MA0.7FA0.3)0.85PbI3 Perovskite and Solar Cell Performance. *Small* **2019**, *15* (9), 1804858.

(11) Gupta, S.; Bendikov, T.; Hodes, G.; Cahen, D. CsSnBr3, A Lead-Free Halide Perovskite for Long-Term Solar Cell Application: Insights on SnF2 Addition. *ACS Energy Lett.* **2016**, *1* (5), 1028−1033.

(12) Li, B.; Long, R.; Xia, Y.; Mi, Q. All-Inorganic Perovskite CsSnBr3 as a Thermally Stable, Free-Carrier Semiconductor. *Angew. Chem., Int. Ed.* **2018**, *57* (40), 13154−13158.
(13) Patel, P. K. Device Simulation of Highly Efficient Eco-Friendly CH3NH3SnI3 Perovskite Solar Cell. *Sci. Rep.* **2021**, *11* (1), 3082.
(14) Díaz-Acosta, C. M.; Martínez-Luévanos, A.; Estrada-Flores, S.; Cano-Salazar, L. F.; Aguilera-González, E. N.; Ibarra-Alonso, M. C. ABX3 Inorganic Halide Perovskites for Solar Cells: Chemical and Crystal Structure Stability. *Matéria* **2021**, *26* (4), No. e13116.
(15) Kumar, M. H.; Dharani, S.; Leong, W. L.; Boix, P. P.; Prabhakar, R. R.; Baikie, T.; Shi, C.; Ding, H.; Ramesh, R.; Asta, M.; Graetzel, M.; Mhaisalkar, S. G.; Mathews, N. Lead-Free Halide Perovskite Solar Cells with High Photocurrents Realized Through Vacancy Modulation. *Adv. Mater.* **2014**, *26* (41), 7122−7127.
(16) Moghe, D.; Wang, L.; Traverse, C. J.; Redoute, A.; Sponseller, M.; Brown, P. R.; Bulović, V.; Lunt, R. R. All Vapor-Deposited Lead-Free Doped CsSnBr3 Planar Solar Cells. *Nano Energy* **2016**, *28*, 469−474.
(17) Wang, A.; Guo, Y.; Muhammad, F.; Deng, Z. Controlled Synthesis of Lead-Free Cesium Tin Halide Perovskite Cubic Nanocages with High Stability. *Chem. Mater.* **2017**, *29* (15), 6493−6501.
(18) Ravidas, B. K.; Roy, M. K.; Samajdar, D. P. Investigation of Photovoltaic Performance of Lead-Free CsSnI3-Based Perovskite Solar Cell with Different Hole Transport Layers: First Principle Calculations and SCAPS-1D Analysis. *Sol. Energy* **2023**, *249*, 163−173.
(19) Seyed-Talebi, S. M.; Mahmoudi, M.; Lee, C.-H. A Comprehensive Study of CsSnI3-Based Perovskite Solar Cells with Different Hole Transporting Layers and Back Contacts. *Micromachines* **2023**, *14* (8), 1562.
(20) Liang, Y.; Cui, X.; Li, F.; Stampfl, C.; Ringer, S. P.; Zheng, R. Electrode-Induced Impurities in Tin Halide Perovskite Solar Cell Material CsSnBr3 from First Principles. *npj Comput. Mater.* **2021**, *7* (1), 63.
(21) Fang, D.; Tong, Y.; Xu, F.; Mi, B.; Cao, D.; Gao, Z. Preparation of CsSnBr3 Perovskite Film and Its All-Inorganic Solar Cells with Planar Heterojunction. *J. Solid State Chem.* **2021**, *294*, 121902.
(22) Tara, A.; Bharti, V.; Sharma, S.; Gupta, R. Device Simulation of FASnI3 Based Perovskite Solar Cell with Zn(O0.3, S0.7) as Electron Transport Layer Using SCAPS-1D. *Opt. Mater.* **2021**, *119*, 111362.
(23) Singh, A. K.; Srivastava, S.; Mahapatra, A.; Baral, J. K.; Pradhan, B. Performance Optimization of Lead Free-MASnI3 Based Solar Cell with 27% Efficiency by Numerical Simulation. *Opt. Mater.* **2021**, *117*, 111193.
(24) Nasrin, T.; Mottakin, M.; Selvanathan, V.; Hossain, M. I.; Shahiduzzaman, Md.; Islam, M. A.; Ahamed, M. S.; Alharbi, H. F.; Akhtaruzzaman, Md. Performance Optimization and Defect Studies of Pb-Free CsSnBr3-Based Perovskite Solar Cells. *Mater. Today Commun.* **2023**, *37*, 107000.
(25) Karmakar, A.; Bhattacharya, A.; Sarkar, D.; Bernard, G. M.; Mar, A.; Michaelis, V. K. Influence of hidden halogen mobility on local structure of $CsSn(Cl_{1-x}Br_x)_3$ mixed-halide perovskites by solid-state NMR. *Chem. Sci.* **2021**, *12* (9), 3253−3263.
(26) Hartmann, C.; Gupta, S.; Bendikov, T.; Kozina, X.; Kunze, T.; Félix, R.; Hodes, G.; Wilks, R. G.; Cahen, D.; Bär, M. Impact of SnF2 Addition on the Chemical and Electronic Surface Structure of CsSnBr3. *ACS Appl. Mater. Interfaces* **2020**, *12* (10), 12353−12361.
(27) Sabba, D.; Mulmudi, H. K.; Prabhakar, R. R.; Krishnamoorthy, T.; Baikie, T.; Boix, P. P.; Mhaisalkar, S.; Mathews, N. Impact of Anionic Br^- Substitution on Open Circuit Voltage in Lead Free Perovskite ($CsSnI_{3-x}Br_x$) Solar Cells. *J. Phys. Chem. C* **2015**, *119* (4), 1763−1767.
(28) Song, T.-B.; Yokoyama, T.; Stoumpos, C. C.; Logsdon, J.; Cao, D. H.; Wasielewski, M. R.; Aramaki, S.; Kanatzidis, M. G. Importance of Reducing Vapor Atmosphere in the Fabrication of Tin-Based Perovskite Solar Cells. *J. Am. Chem. Soc.* **2017**, *139* (2), 836−842.
(29) Kumar, A.; Pandey, N.; Punetha, D.; Saha, R.; Chakrabarti, S. Enhancement in the Structural and Optical Properties after Incorporation of Reduced Graphene Oxide (RGO) Nanocomposite in Pristine CsSnBr3 for Solar Cell Application. *ACS Appl. Electron. Mater.* **2023**, *5* (6), 3144−3153.
(30) Burgelman, M.; Nollet, P.; Degrave, S. Modelling Polycrystalline Semiconductor Solar Cells. *Thin Solid Films* **2000**, *361−362*, 527−532.
(31) Hossain, M. K.; Rubel, M. H. K.; Toki, G. F. I.; Alam, I.; Rahman, M. F.; Bencherif, H. Effect of Various Electron and Hole Transport Layers on the Performance of CsPbI3-Based Perovskite Solar Cells: A Numerical Investigation in DFT, SCAPS-1D, and WxAMPS Frameworks. *ACS Omega* **2022**, *7* (47), 43210−43230.
(32) Hossain, M. K.; Toki, G. F. I.; Samajdar, D. P.; Mushtaq, M.; Rubel, M. H. K.; Pandey, R.; Madan, J.; Mohammed, M. K. A.; Islam, M. R.; Rahman, M. F.; Bencherif, H. Deep Insights into the Coupled Optoelectronic and Photovoltaic Analysis of Lead-Free CsSnI3 Perovskite-Based Solar Cell Using DFT Calculations and SCAPS-1D Simulations. *ACS Omega* **2023**, *8* (25), 22466−22485.
(33) Chen, L.-J.; Lee, C.-R.; Chuang, Y.-J.; Wu, Z.-H.; Chen, C. Synthesis and Optical Properties of Lead-Free Cesium Tin Halide Perovskite Quantum Rods with High-Performance Solar Cell Application. *J. Phys. Chem. Lett.* **2016**, *7* (24), 5028−5035.
(34) Jiang, M.; Tang, J. Simulated Development and Optimized Performance of Narrow-Bandgap CsSnI3-Based All-Inorganic Perovskite Solar Cells. *J. Phys. D Appl. Phys.* **2021**, *54* (46), 465104.
(35) Lin, S.; Zhang, B.; Lü, T. Y.; Zheng, J.-C.; Pan, H.; Chen, H.; Lin, C.; Li, X.; Zhou, J. Inorganic Lead-Free B-γ-CsSnI3 Perovskite Solar Cells Using Diverse Electron-Transporting Materials: A Simulation Study. *ACS Omega* **2021**, *6* (40), 26689−26698.
(36) Pindolia, G.; Shinde, S. M.; Jha, P. K. Optimization of an Inorganic Lead Free RbGeI3 Based Perovskite Solar Cell by SCAPS-1D Simulation. *Sol. Energy* **2022**, *236*, 802−821.
(37) Shalenov, E. O.; Dzhumagulova, K. N.; Seitkozhanov, Y. S.; Ng, A.; Valagiannopoulos, C.; Jumabekov, A. N. Insights on Desired Fabrication Factors from Modeling Sandwich and Quasi-Interdigitated Back-Contact Perovskite Solar Cells. *ACS Appl. Energy Mater.* **2021**, *4* (2), 1093−1107.
(38) Jamal, M. S.; Shahahmadi, S. A.; Abdul Wadi, M. A.; Chelvanathan, P.; Asim, N.; Misran, H.; Hossain, M. I.; Amin, N.; Sopian, K.; Akhtaruzzaman, Md. Effect of Defect Density and Energy Level Mismatch on the Performance of Perovskite Solar Cells by Numerical Simulation. *Optik* **2019**, *182*, 1204−1210.
(39) Haider, S. Z.; Anwar, H.; Wang, M. A Comprehensive Device Modelling of Perovskite Solar Cell with Inorganic Copper Iodide as Hole Transport Material. *Semicond. Sci. Technol.* **2018**, *33* (3), 035001.
(40) Soucase, B. M.; Guaita Pradas, I.; Adhikari, K. R. Numerical Simulations on Perovskite Photovoltaic Devices. *Perovskite Materials−Synthesis, Characterisation, Properties, and Applications*; InTech, 2016..
(41) Chowdhury, M. S.; Shahahmadi, S. A.; Chelvanathan, P.; Tiong, S. K.; Amin, N.; Techato, K.; Nuthammachot, N.; Chowdhury, T.; Suklueng, M. Effect of Deep-Level Defect Density of the Absorber Layer and n/i Interface in Perovskite Solar Cells by SCAPS-1D. *Results Phys.* **2020**, *16*, 102839.
(42) Jensen, N.; Hausner, R. M.; Bergmann, R. B.; Werner, J. H.; Rau, U. Optimization and Characterization of Amorphous/Crystalline Silicon Heterojunction Solar Cells. *Prog. Photovoltaics* **2002**, *10* (1), 1−13.
(43) Huang, L.; Sun, X.; Li, C.; Xu, R.; Xu, J.; Du, Y.; Wu, Y.; Ni, J.; Cai, H.; Li, J.; Hu, Z.; Zhang, J. Electron Transport Layer-Free Planar Perovskite Solar Cells: Further Performance Enhancement Perspective from Device Simulation. *Sol. Energy Mater. Sol. Cells* **2016**, *157*, 1038−1047.
(44) Otoufi, M. K.; Ranjbar, M.; Kermanpur, A.; Taghavinia, N.; Minbashi, M.; Forouzandeh, M.; Ebadi, F. Enhanced Performance of Planar Perovskite Solar Cells Using TiO2/SnO2 and TiO2/WO3 Bilayer Structures: Roles of the Interfacial Layers. *Sol. Energy* **2020**, *208*, 697−707.
(45) Meng, G.; Elumalai, N. K.; Mehdizadeh-Rad, H.; Ram, K. S.; Setsoafia, D. D. Y.; Ompong, D. Investigating the Impact of Interfacial

https://doi.org/10.1021/acs.energyfuels.4c00953
Energy Fuels 2024, 38, 8229−8248

Layers on Device Performance of Highly Stable Cs2InBiBr6 Based Double Perovskite Solar Cells. *Adv. Theory Simul.* **2024**, *7* (2), 2300784.
(46) Khatoon, S.; Kumar Yadav, S.; Chakraborty, V.; Singh, J.; Bahadur Singh, R. A Simulation Study of All Inorganic Lead-Free CsSnBr3 Tin Halide Perovskite Solar Cell. *Mater. Today Proc.* **2023**, DOI: 10.1016/j.matpr.2023.04.167.

https://doi.org/10.1021/acs.energyfuels.4c00953
Energy Fuels 2024, 38, 8229−8248